Economic Geology, v. 108, pp. 667–690

Biotite and Apatite as Tools for Tracking Pathways of Oxidized Fluids in the Archean East Repulse Gold Deposit, Australia

Adam B. Bath,[1,†] John L. Walshe,[1] Jonathan Cloutier,[1] Micheal Verrall,[1] James S. Cleverley,[1] Mark I. Pownceby,[2] Colin M. Macrae,[2] Nick C. Wilson,[2] Janet Tunjic,[3,*] Gustav S. Nortje,[4,*] and Philip Robinson[5]

[1] *CSIRO Earth Science and Resource Engineering, P.O. Box 1130 Bentley, Western Australia 6102, Australia*

[2] *CSIRO Process Science and Engineering, Clayton Laboratories, Bayview Avenue, Clayton, Victoria 3168, Australia*

[3] *Gold Fields Limited, Level 1, 62 Colin Street, West Perth, Western Australia 6005, Australia*

[4] *Newcrest Mining Limited, 400 George St., Brisbane, Queensland 4000, Australia*

[5] *CODES ARC Centre of Excellence in Ore Deposits, University of Tasmania, Private Bag 126, Hobart, Tasmania 7001, Australia*

Abstract

Fluid pathways in hydrothermal ore deposits can potentially be traced through alteration zoning patterns and the chemistry of mineral phases (i.e., major, trace elements, and isotopic composition), which provide insight into the physico-chemical gradients within and adjacent to pathways. World-class Neoarchean gold deposits of the eastern Yilgarn can be zoned with respect to alteration assemblages, but in many cases fluid pathways are poorly understood, which makes it difficult to identify the nature and source of fluids. This study conducted detailed core logging, SEM mineral mapping of alteration assemblages, and microprobe analysis of biotite and apatite in order to identify chemical gradients across the East Repulse gold deposit of the St. Ives gold camp, eastern Yilgarn, Western Australia. Results show that the East Repulse deposit is vertically zoned with relatively oxidized sulfate-rich alteration in the footwall of the deposit (anhydrite, celestine and/or barite), sulfide-rich alteration in the core of the deposit (pyrite ± magnetite with minor barite and celestine), and relatively reduced sulfide-only assemblages (pyrite ± pyrrhotite with minor pentlandite, millerite, and cobaltite) in the hanging wall of the deposit. Gold was identified as inclusions in pyrite and associated biotite implying a link between biotite-pyrite alteration and gold mineralization. The abundance of F in biotite and apatite progressively decreases from the footwall of the deposit into the mineralized core. This trend of decreasing F in biotite and apatite with decreasing depth is consistent with an hypothesis that oxidized F- and K-bearing fluids were focused along subvertical pathways beneath the deposit, within or subjacent to granitoid dikes. The biotite-apatite geothermometer shows that these fluids were relatively hot (~480° ± 60°C) at the time of alteration. These relatively high temperature, oxidized, F- and K-bearing fluids may have been derived from a proximal magmatic source.

Introduction

Neoarchean gold deposits of the eastern Yilgarn goldfields are world-class deposits, with the St. Ives gold camp alone containing more than 12 million ounces (Moz) of gold (Miller et al., 2010). These deposits have been classified as orogenic gold deposits and are considered to have formed as a result of focused fluid flow during late active deformation and metamorphism of volcano-plutonic terranes (Groves et al., 1998, 2003, 2005; Kerrich et al., 2000; Cox and Ruming, 2004; Weinberg et al., 2004, 2005; Weinberg and van der Borgh, 2008). However, the architecture of crustal-scale flow systems at the time of gold mineralization is poorly understood (Groves et al., 2003), although Neumayr et al. (2008) suggested that deposit- and camp-scale mineral zoning broadly constrained the fluid regime in the St. Ives gold camp. They identified lateral and vertical zoning from oxidized alteration domains (magnetite-pyrite, hematite-pyrite) to reduced domains (pyrrhotite-pyrite) across gold deposits and proposed that redox gradients played a key role in the deposition of gold. It remains unclear, however, how alteration patterns specifically relate to fluid pathways in gold systems, and this gap in knowledge limits our understanding of the processes controlling gold transportation and deposition. Here the halogen content of biotite and apatite was investigated to test if a fluid pathway(s) could be identified which links high-grade gold zones of the East Repulse gold deposit with oxidized (anhydrite ± magnetite) alteration assemblages in the footwall. Recognition of such pathways will enhance the ability to identify fluid sources and will help to facilitate accurate crustal fluid-flow modeling and potentially help explorers identify new targets.

The compositions of biotite and apatite are sensitive to the physico-chemical conditions of the hydrothermal system, such as activity of halogens, oxidation and sulfidation states, pH, volatile phase exsolution, element complexing, and partitioning at temperature and pressure (Webster, 1997, 2004; Cleverley, 2006; Boomeri et al., 2009, 2010). The substitution of F and Cl into hydroxyl sites of biotite and apatite is controlled by the activity of HF and HCl in the hydrothermal fluids as well as the composition of the mica, pressure, and temperature (Munoz and Ludington, 1977; Munoz and Swenson, 1981; Munoz, 1984; Zhu and Sverjensky, 1991; Boomeri et al., 2009, 2010). The halogen content of biotite has been used to infer the direction of fluid-flow based on the hypothesis that evolving fluids may become depleted in F through the preferential partitioning of F into mineral phases (Gunow et al.,

† Corresponding author: e-mail address, Adam.Bath@csiro.au

* Former address: St. Ives Gold Mining Company (Pty) Limited, P.O. Box 359, Kambalda West, Western Australia 6442, Australia.

Submitted: January 5, 2012
Accepted: July 23, 2012

1980). This method has proved useful in understanding the fugacity of halogens relative to water fugacity, temperature, and fluid pathways in porphyry environments (Beane, 1974; Boomeri et al., 2009, 2010), but so far this method has not been applied to alteration assemblages from Neoarchean gold deposits. As biotite is a common alteration phase of Archean gold deposits (e.g., St. Ives camp and Wattle Dam), this type of data may be applicable to numerous other systems in the region.

Regional- and Camp-Scale Geology

Gold mineralization in the Kalgoorlie terrane is thought to have occurred over an extended period between ca. 2665 and 2630 Ma (e.g., Yeats et al., 1999; Czarnota et al., 2010). Gold deposits occur in a wide variety of host rocks, including mafic and ultramafic volcanic rocks, granitoids, and late basin siliclastics. Some of the most significant resources historically occur in dolerite intrusions (e.g., Golden Mile; Bateman and Hagemann, 2004). Economic accumulations of gold may be associated with a diverse array of minerals and mineral assemblages. A common association is quartz in narrow veins, with metasomatic carbonate ± albite ± sulfide. However significant gold resources occur in the absence of this assemblage. For example the high-grade Wattle Dam deposit is hosted in amphibole ± biotite-altered ultramafic rocks (Hutchison, 2011).

The East Repulse deposit occurs within the Victory-Defiance Complex, St. Ives gold camp, which is located approximately 15 km south-southeast of Kambalda, Western Australia (Fig. 1). Rocks of the St. Ives camp form part of the Norseman-Wiluna greenstone belt of the Kalgoorlie terrane, which may have formed in a back-arc setting between 2715 and 2650 Ma (Swager, 1997; Blewett et al., 2010; Czarnota et al., 2010; Squire et al., 2010). Stratigraphically, the Kalgoorlie terrane is divided into (1) mafic to ultramafic volcanic and intrusive rocks of the Kambalda sequence (~2710–2690 Ma);

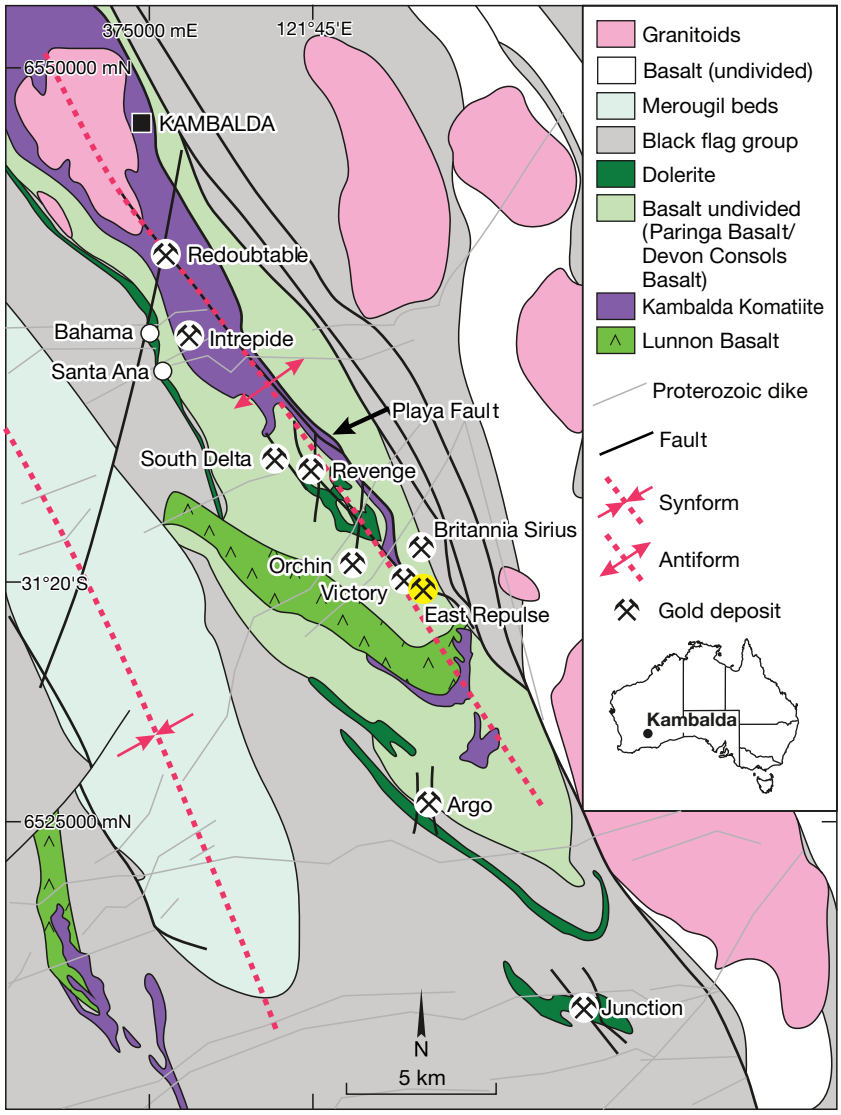

FIG. 1. Geologic map of the St. Ives gold camp, showing the location of the East Repulse deposit relative to other major gold deposits (modified from Neumayr et al., 2008).

(2) intermediate to felsic volcaniclastic successions of the Kalgoorlie sequence (2690–2665 Ma; Black Flag Group) and (3) the siliciclastic packages of the late basin sequence (2665–2650 Ma; Merougil Beds; Fig. 1; Blewett et al., 2010). The Kambalda sequence is intruded by intermediate to felsic intrusions, which commonly show ages of ca. 2670 and 2630 Ma (Nelson, 1997; Watchorn, 1998; Yeats et al., 1999; Neumayr et al., 2008; Camp, 2011). Rocks of the Kambalda sequence have been metamorphosed to upper greenschist and lower amphibolite facies, and contain assemblages of plagioclase and amphibole. These rocks have sustained at least four main deformation events between ca. 2700 and 2630 Ma (Swager, 1997).

Deposit-Scale Geology

The East Repulse deposit is hosted in a sequence of mafic and ultramafic volcanic and intrusive rocks, with minor interflow sediments. Lithostratigraphic units of the deposit belong to the Kambalda sequence which comprises Kambalda Komatiite, Devon Consols Basalt, and Paringa Basalt in the studied area (Fig. 2A, B; Swager, 1997; Kositcin et al., 2008). An extensive interflow sedimentary unit, the Kapai Slate, occurs between the Devon Consols and Paringa Basalts. Thin lenses of magnetite-quartz rock occur within the Devon Consols Basalt within the studied section of the East Repulse deposit. It is unclear if these represent altered interflow sediments or if they formed as a result of hydrothermal alteration. Here magnetite-quartz–rich lenses are inferred to be altered Kapai Slate (Fig. 2B).

The lithostratigraphic units of the Kambalda sequence are intruded by the Defiance Dolerite and minor lamprophyre intrusions (comprised of biotite, amphibole, and feldspar). They are also intruded by quartz-plagioclase-K-feldspar tonalite to granodiorite and plagioclase-K-feldspar phyric trondhjemite dikes, which are collectively referred to as "granitoids." The quartz-plagioclase ± K-feldspar phyric tonalite to granodiorite

FIG. 2. A. Geologic map of the area surrounding the East Repulse deposit, showing the location of major gold deposits, as well as the location of the studied cross section shown in (B) (modified from Watchorn, 1998). B. A south-north geologic cross section of the East Repulse deposit. Samples analyzed in this study were collected from diamond drill holes along this section.

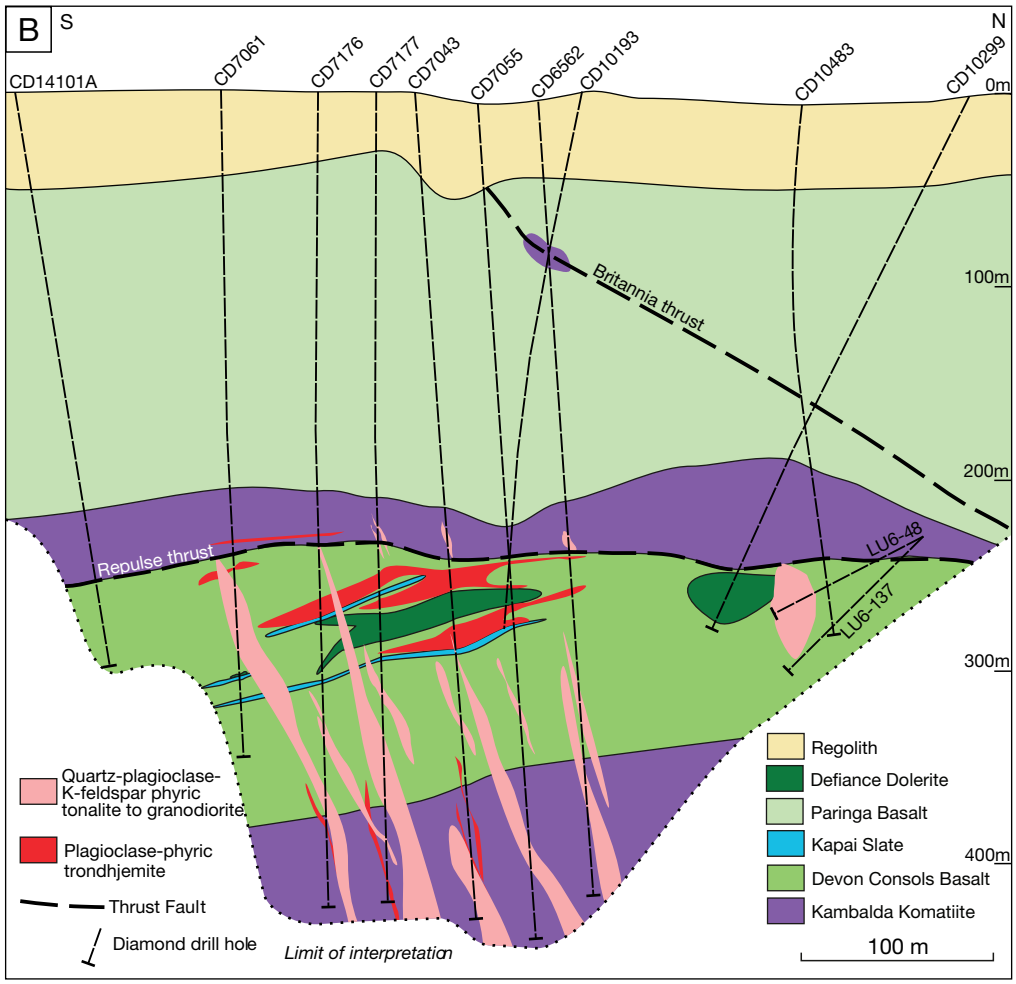

FIG. 2. *(Cont.)*

dikes crop out in the Leviathan pit, which occurs to the northwest of the East Repulse deposits. There tonalite to granodiorite dikes are near vertically dipping to steeply east dipping and strike northwest in the footwall and north in the hanging wall of the East Repulse shear zone (pers. commun., J. Donaldson, 2011).

Alteration and Mineralization

The Victory and Defiance deposits (Fig. 2A) formed in a dominantly oxidized alteration domain, as defined by Neumayr et al. (2008). The Conqueror deposit on the southwestern side of the complex formed in a dominantly reduced domain that is replicated on the eastern side of the complex, outboard of the East Repulse deposit (Neumayr et al., 2008). Coherent patterns of trace Bi and Mo enrichment in altered rocks aid definition of the oxidized domain that has a sharply defined eastern boundary against the Playa-Repulse fault (Prendergast, 2007).The East Repulse deposit sits immediately below this camp-scale redox boundary.

Gold mineralization within the East Repulse deposit occurs at a depth of about 220 m below the present surface (at >0.5 g/t Au; Fig. 3). Discrete higher grade mineralized zones (i.e., >1 g/t Au), which are commonly less than 50 m in diameter, occur beneath the Repulse thrust. Gold mineralization can be traced to depths of at least ~400 m, and in these domains gold mineralization occurs in altered granitoids and adjacent mafic and ultramafic wall rocks.

Based on crosscutting and overprinting relationships, three dominant stages of alteration have been established relative to mineralization. These include (1) early-stage albite-carbonate (± sulfates, sulfides, magnetite and/or epidote); (2) main-stage biotite-amphibole-carbonate (± anhydrite, pyrite and/or gold) and (3) late-stage carbonate (± albite, quartz, pyrite, chlorite, epidote and/or clinozoisite) alteration (Fig. 4). These stages of alteration overprint Kambalda Komatiite, Devon Consols Basalt, Paringa Basalt, Defiance Dolerite, Kapai Slate and granitoids. Thin lamprophyre intrusions (<1 m thick in drill core) appear to cut altered and mineralized rocks in some areas.

Alteration assemblages of the East Repulse deposit have been divided into domains that reflect lithology and the zoning of alteration assemblages from the footwall through to the hanging wall of the deposit (Figs. 4, 5A, B). The five alteration domains include (1) a lower domain, (2) a granitoid domain, (3) an ore domain, (4) a transitional domain, and (5) an upper domain. The lower domain occurs in the footwall of the deposit, the ore domain occurs in the core of the deposit, and the upper and transitional domains occur in the hanging wall.

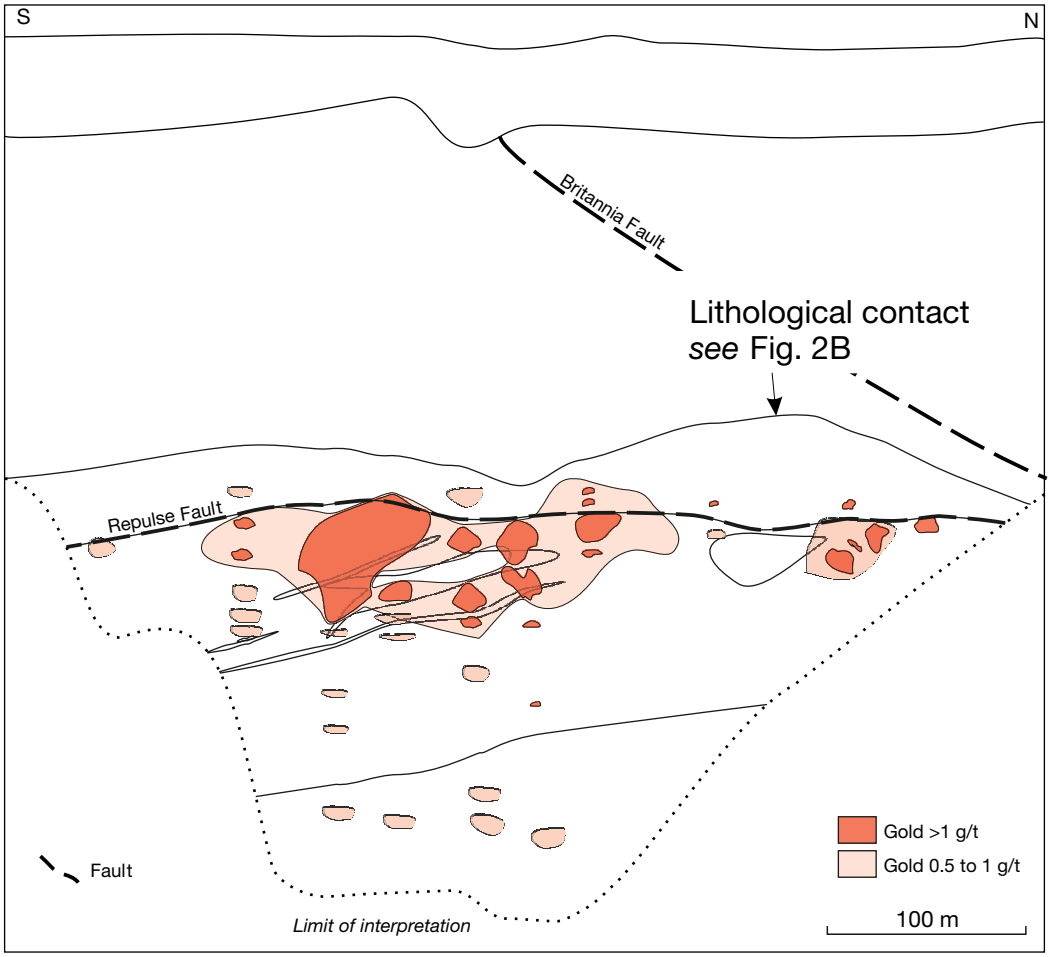

FIG. 3. South-north cross section of the East Repulse deposit (location shown in Fig. 2A), showing gold grades relative to lithologic and inferred structural contacts.

Rocks belonging to the granitoid domain were identified in the footwall, core, and hanging wall of the deposit.

The above alteration domains are in part based on the assemblage of minor minerals associated with the various stages of alteration. These minor mineral phases were identified using the SEM (Philips XL 40) on samples collected at 10-m intervals from numerous diamond drill holes shown on the cross section in Figure 2. Mineral Liberation Analysis (MLA) software was used to drive the SEM and to identify mineral phases with a higher backscattered reflectance than pyrite. Results show that the ore and granitoid domains include very similar types of minor mineral phases (Fig. 5A). These phases include early- and late-stage barite and celestine, and main-stage scheelite, molybdenite, monazite, and galena (Fig. 4). In contrast the lower domain may include one or several of these phases of the ore and granitoid domains; however, their distribution is more random in the lower domain. The transitional domain is marked by a notable change in the minor mineral phases. In particular, sulfate minerals are rare, and scheelite and molybdenite were not identified in these rocks (Fig. 5A). In contrast, some samples contained bismuthinite, galena, and nickel sulfides, which were all associated with main-stage alteration. Nickel sulfides (pentlandite, millerite, and siegenite) were all identified in the upper domain (Fig. 5A, B). These minerals are associated with both biotite and clinozoisite (Fig. 4).

Lower domain

The lower domain, beneath the ore domain, occurs within the Devon Consols Basalt and Kambalda Komatiite. Early-stage calcic alteration is developed in the Devon Consols Basalt. The alteration is locally texturally destructive with epidote alteration overprinting metamorphic assemblages dominated by plagioclase and amphibole (Fig. 6A-D). This stage of alteration has been crosscut by veins of albite (An <10)-carbonate (late-stage), which contain traces of apatite and molybdenite (Fig. 6B, E).

Main-stage alteration in the lower domain comprises assemblages of biotite-amphibole-anhydrite ± calcite ± pyrite (Fig. 6A, F, G). Main-stage alteration is pervasive in some areas but also occurs as veins with anhydrite and quartz in the Devon Consols Basalt and Kambalda Komatiite (Fig. 6A). Biotite alteration is well developed in the Devon Consols Basalt adjacent to granitoid intrusions. In these areas biotite alteration also occurs with carbonate, titanite, rutile, quartz, and traces of scheelite. Gypsum within the Devon Consols Basalt commonly leaches or is pseudomorphous after primary anhydrite, which is best preserved in veins within the Kambalda Komatiite (Fig. 6F).

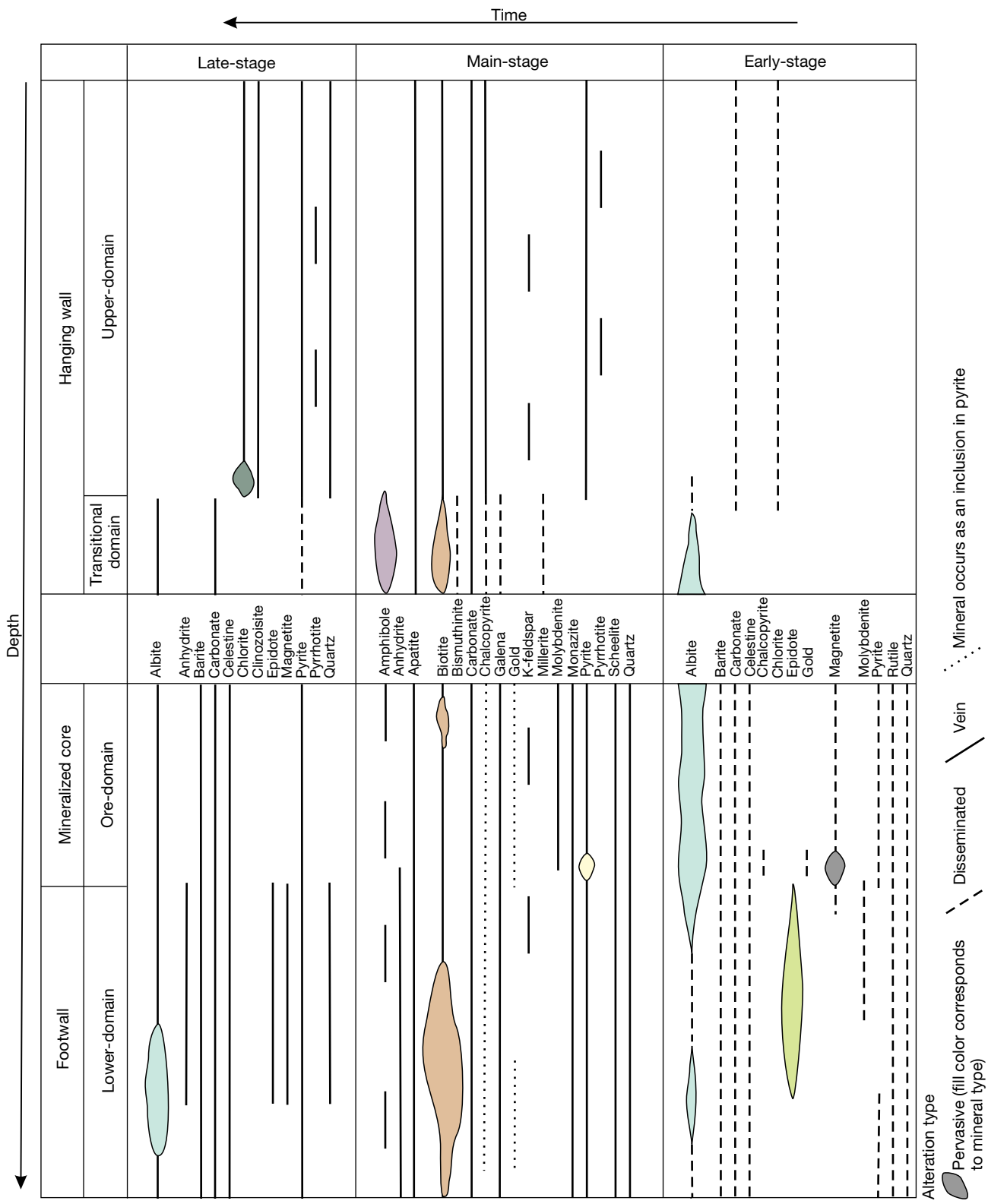

FIG. 4. Time-space paragenetic diagram for the East Repulse deposit. The three stages of alteration are inferred to broadly represent the major alteration events. The figure also illustrates the styles of alteration in the hanging wall, core, and footwall of the deposit (e.g., pervasive, vein, and disseminated).

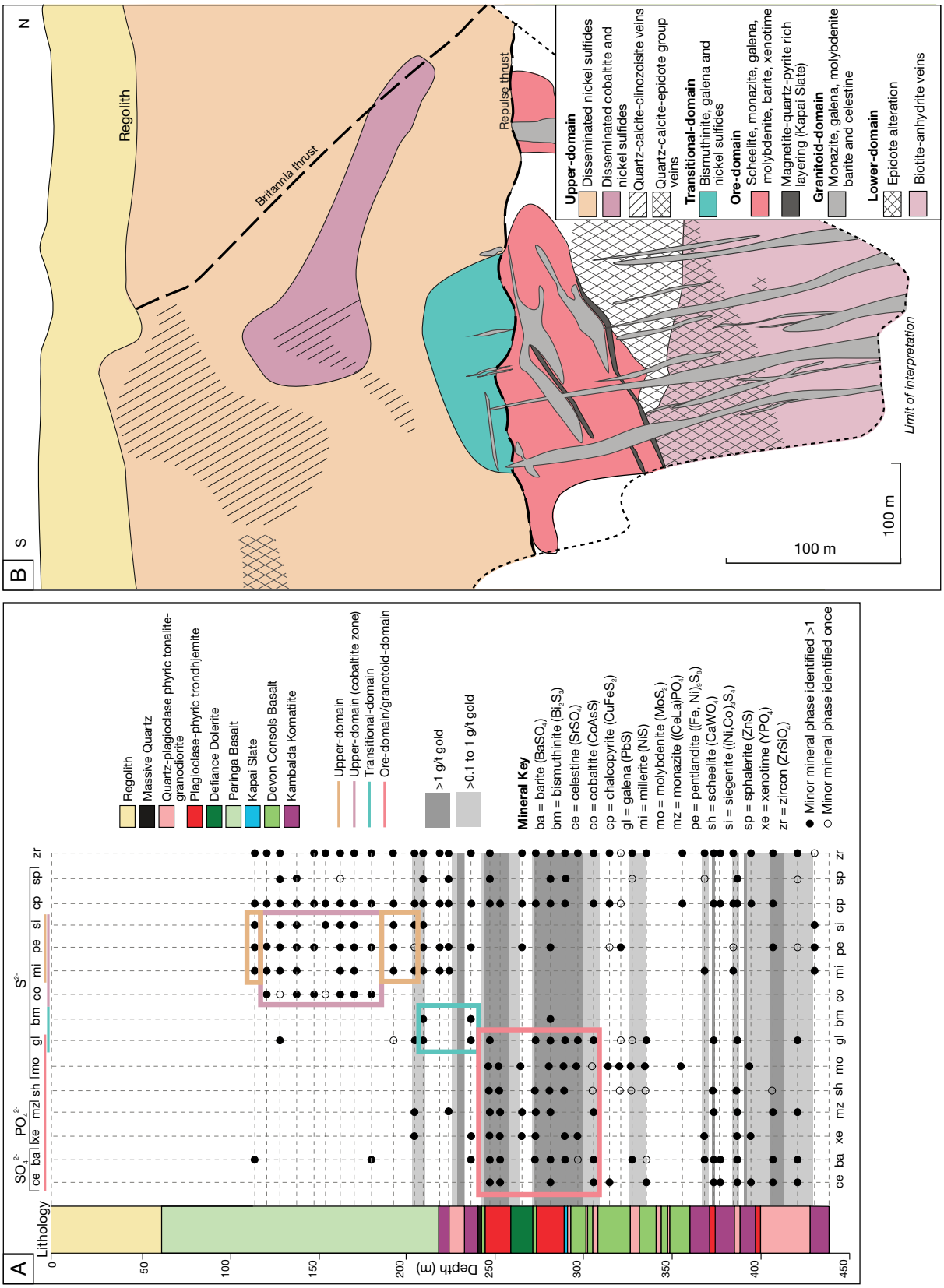

FIG. 5. A. Diamond drill hole log of CD7043 (see Fig. 2B), showing lithology, gold grades, alteration domains, and the distribution of selected minor mineral phases. Characteristics of domains include (1) an upper domain composed of nickel sulfides and cobaltite; (2) transitional domain characterized by bismuthinite, galena, and nickel sulfides; (3) ore and granitoid domains which comprise celestine, scheelite, barite, molybdenite, monazite, and galena (4) a lower domain that sparsely includes celestine, scheelite barite, molybdenite, and galena. Mineral phases were identified via SEM mapping of polished rock slabs (25 mm in size). B. A south-north cross section of the East Repulse deposits, showing the distribution of the various alteration domains, which have been delineated using alteration assemblages from minor and major minerals.

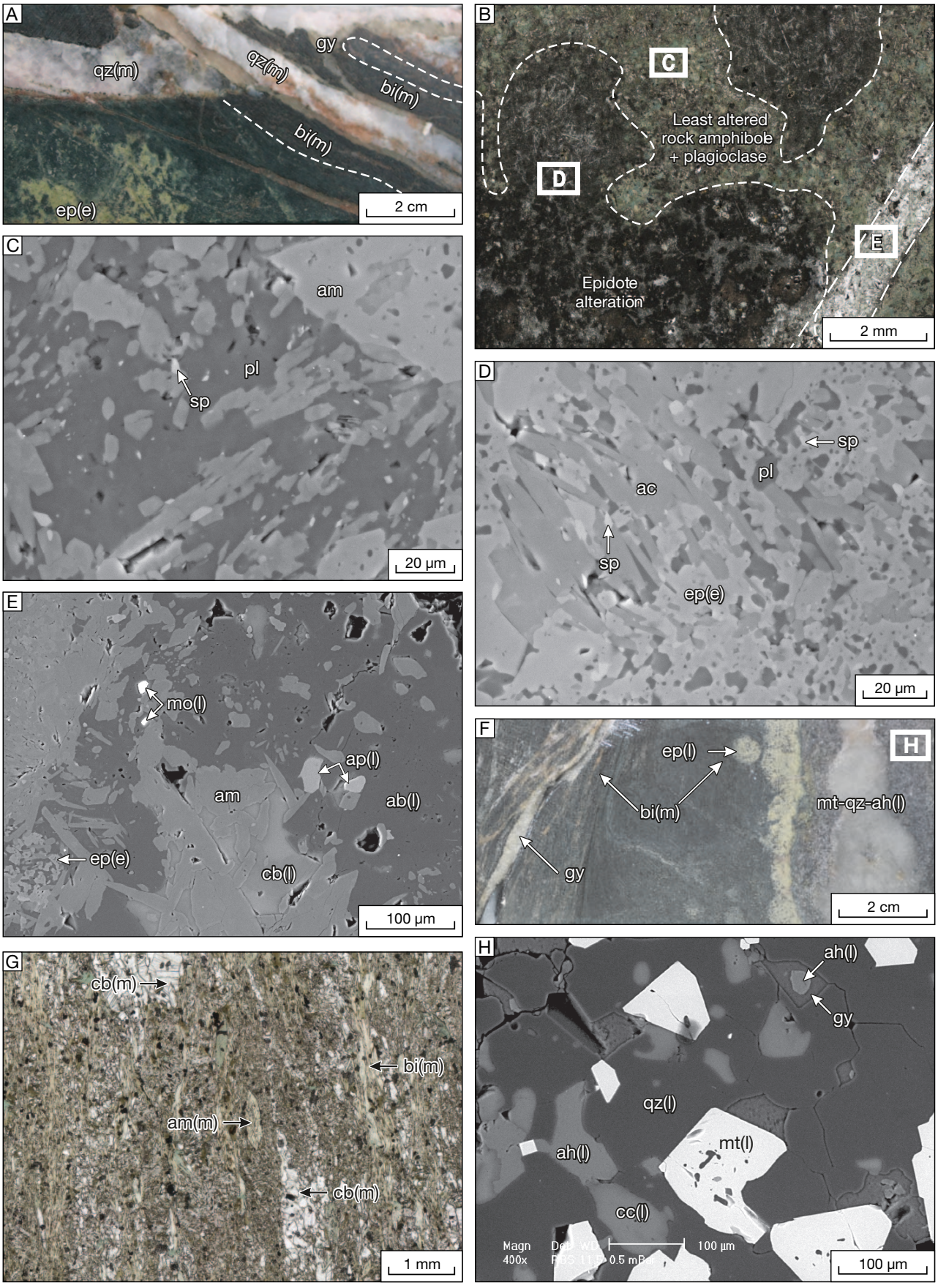
A
qz(m)
qz(m)
gy
bi(m)
bi(m)
ep(e)
2 cm
B
C
D
E
Least altered
rock amphibole
+ plagioclase
Epidote
alteration
2 mm
C
am
pl
sp
20 µm
D
sp
pl
ac
sp
ep(e)
20 µm
E
mo(l)
ap(l)
am
ab(l)
ep(e)
cb(l)
100 µm
F
H
ep(l)
bi(m)
mt-qz-ah(l)
gy
2 cm
G
cb(m)
bi(m)
am(m)
cb(m)
1 mm
H
ah(l)
gy
qz(l)
mt(l)
ah(l)
cc(l)
Magn
400x
100 µm
100 µm

Late-stage alteration in the lower domain occurs in the Devon Consols Basalt as veins comprising quartz-magnetite-anhydrite-epidote-carbonate overprint main-stage biotite-anhydrite veins (Fig. 6F). Late-stage epidote alteration is either pervasive and/or occurs as selvages around veins that comprise <0.3-mm quartz, magnetite, calcite, and anhydrite (Fig. 6F, H).

Granitoid domain

Early-stage alteration in the granitoid domain is characterized by plagioclase phenocrysts (~An_{30}) replaced by albite (~An_5), which has produced a fine-grained texture (Fig. 7A-E). The <200-μm-size albite is porous (Fig. 7D-E). Pores are partly filled with carbonate, pyrite, barite, and celestine.

Main-stage biotite-pyrite veins crosscut early-stage albite and carbonate (Figs. 7C, 8A). These veins include monazite, minor amounts of anhydrite, barite, pyrite, calcite, and traces of electrum (Au:Ag $\approx$ 3:7; Fig. 7F). A minor amount of K-feldspar is associated with biotite alteration in granitoid dikes. Main-stage biotite is overprinted by late-stage quartz-albite-carbonate-pyrite alteration, which occurs as veins and/or as local pervasive alteration (Fig. 8A). The albitization commonly overprints a deformation fabric in the granitoids defined by the alignment of main-stage biotite in some areas.

Ore domain

Alteration assemblages of the Devon Consols Basalt and Defiance Dolerite are characterized by locally pervasive albite-carbonate-barite-celestine-magnetite (early-stage), which is crosscut by main-stage biotite-pyrite stringers (Fig. 8A, B). Main-stage veins have been crosscut by late-stage carbonate-albite ± quartz veins (Fig. 8A-C). Gold mineralization in the ore domain occurs as inclusions in main-stage pyrite and biotite (Fig. 8D, E). Visible gold, apatite, and silver tellurides were identified as inclusions in main-stage pyrite, biotite and/or quartz. Bismuthinite, sphalerite, galena, chalcopyrite, rutile, ilmenite, monazite, and scheelite also occur as inclusions in main-stage pyrite or coexist in quartz veins (Fig. 8F), indicating that these minerals likely crystallized during main-stage alteration.

Transitional domain

The transitional domain occurs in the hanging wall of the ore deposit in the Paringa Basalt and Kambalda Komatiite. The Paringa Basalt and parts of the Kambalda Komatiite show pervasive main-stage amphibole-biotite alteration, with medium-grained amphibole intergrown with biotite (Fig. 9A-D). Amphibole contains inclusions of bismuthinite, millerite, pentlandite, galena, and sphalerite (Fig. 9D). Amphibole-biotite–altered Paringa Basalts are also crosscut by carbonate-amphibole-albite-pyrite veins, which are inferred to be related to late-stage alteration (Fig. 9A-B). Late-stage pyrite overprints and contains inclusions of main-stage biotite and amphibole (Fig. 9A-B). The occurrence of bismuthinite in main-stage amphibole indicates that bismuthinite, Ni sulfides, galena, and sphalerite either formed prior to or during main-stage alteration.

The Kambalda Komatiite in the transitional domain also contains localized zones of pervasive talc-chlorite-carbonate alteration. These zones appear to be crosscut by biotite-amphibole-carbonate alteration and may reflect an earlier stage of alteration within the transitional domain.

Upper domain

The upper domain is hosted in the Paringa Basalt. The Paringa Basalt is a meta-basalt that comprises amphibole, plagioclase, and spotty biotite, which is overprinted by numerous stages of alteration. Alteration stages are difficult to link with those in other domains. In particular notable sharp changes in alteration assemblages occur between the transitional and the upper domains (Fig. 4). These changes are consistent with an alteration front that separates two distinct camp-scale alteration domains (Neumayr et al., 2008). Movement of the upper-domain block relative to other domains following alteration and mineralization is not discounted.

In the upper domain the earliest stage of alteration is chlorite-carbonate alteration (early-stage?), which overprints metamorphic amphibole, plagioclase, and biotite. Chlorite-carbonate alteration is overprinted by main-stage(?) biotite alteration, and chlorite-altered rocks have been crosscut by veins of K-feldspar-calcite-biotite-pyrite with traces of millerite and chalcopyrite (main-stage (?); Fig. 10A-B). There also appears to be a late-stage(?) chlorite alteration event that overprints metamorphic and/or main-stage(?) biotite. There are also quartz-clinozoisite/epidote-pyrite-calcite-chlorite veins and disseminated clinozoisite and pyrite ± pyrrhotite alteration, which are considered to be a part of late-stage(?) alteration

FIG. 6. Typical lower domain alteration assemblages. A. Diamond drill core of lower domain Devon Consols Basalt, which has been altered by early-stage epidote and crosscut by main-stage quartz-anhydrite veins with biotite selvages (DDH CD7043-361.7m). B. Early-stage epidote alteration is crosscut by a late-stage albite-carbonate vein in Devon Consols Basalt. Devon Consols Basalt sample is from the lower domain and is viewed in plane-polarized light. White squares denote areas where images for (C), (D), and (E) were taken from DDH CD7055-326.45m. C. Backscattered electron image of least altered area of Devon Consols Basalt as shown in (B). Least altered zones consist of subhedral amphibole and anhedral plagioclase. Small inclusions of sphene are common in plagioclase and amphibole. D. Backscattered electron image of early-stage epidote-altered Devon Consols Basalt as shown in (B). Early-stage epidote preferentially has replaced plagioclase and partially replaced amphibole. E. Backscattered electron image of late-stage(?) albite-carbonate vein as shown in (B). The vein also contains amphibole as well as traces of molybdenite and apatite. F. Diamond drill core of Devon Consols Basalt overprinted by main-stage biotite alteration, which has been overprinted by late-stage epidote selvage of a quartz-magnetite-anhydrite-calcite vein. White square denotes area where (H) was collected from DDH CD7061-330.4m. G. Main-stage biotite-amphiole-calcite alteration of Devon Consols Basalt in plane-polarized light (DDH CD7055-294.8m). H. Backscattered electron image of a late-stage quartz-magnetite-anhydrite-calcite vein, which crosscuts Devon Consols Basalt in the lower domain as shown in (F). Mineral abbreviations for Figures 6–10: ab = albite, ak = ankerite, am = amphibolite, au = gold/electrum, ba = barite, bi = biotite, bm = bismuthinite, cb = carbonate, ch = chlorite, cp = chalcopyrite, cz = clinozoisite, il = ilmenite, mt = magnetite, mi = millerite, pl = plagioclase, py = pyrite, ru = rutile, sp = sphene, sh = scheelite, qz = quartz. Letters in parentheses represent inferred stage of alteration: early-stage = (e), main-stage = (m) and late-stage = (l).

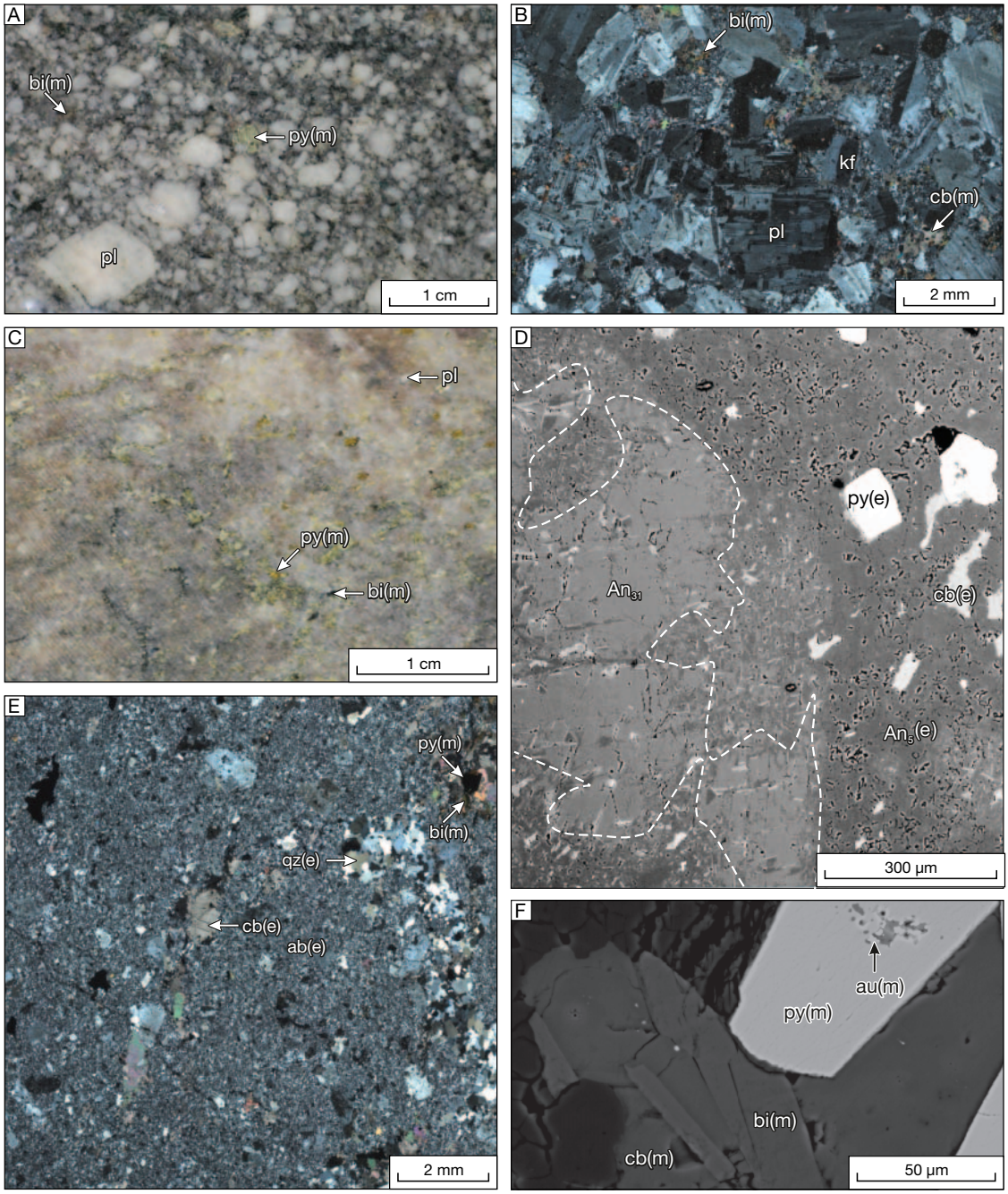

FIG. 7. Alteration assemblages of the granitoid domain. A. Diamond drill hole of biotite- and albite-altered plagioclase-phyric trondhjemite, which intrudes rocks of the lower domain. The sample includes milky white plagioclase phenocrysts with interstitial early-stage fine-grained albite and carbonate, and main-stage biotite-pyrite-carbonate alteration (DDH CD7055-399.9m). B. Biotite- and albite-altered plagioclase-phyric trondhjemite in cross-polarized light (same sample as (A)). Plagioclase phenocrysts show multiple twinning. Some phenocrysts also show simple twinning, which is consistent with K-feldspar. Patches of early-stage fine-grained albite-carbonate and main-stage biotite-pyrite-carbonate alteration occur in the interstitial to feldspar phenocrysts. C. Diamond drill hole of pervasively early-stage albite-altered plagioclase-phyric trondhjemite from the ore domain area. The sample also contains thin veins of main-stage biotite, pyrite, and carbonate. D. Backscattered image of andesine (~An_{30}) partially replaced by early-stage albite (~An_5) from a quartz-plagioclase-phyric tonatile to granodiorite intrusion. The parent andesine has a relatively smooth textured surface, whereas the albite has pores (black). The albite also contains pores filled with barite and is intergrown with pyrite and carbonates, which are inferred to have been deposited during sodic-calcic alteration (DDH CD7043-373.0m). E. Pervasively albite-altered plagioclase-phyric trondhjemite as shown in (D) in cross-polarized light. The sample has been completely recrystallized to fine-grained albite, carbonate, and quartz during early-stage alteration. The sample also includes patches of biotite and pyrite alteration, which are inferred to have been deposited during main-stage alteration. F. Backscattered electron image of main-stage biotite-calcite-pyrite alteration within a granitoid host rock. The image also shows that inclusions of electrum occur in main-stage pyrite (DDH CD7043-373.0m). Abbreviation An_x refers to anorthite component of plagioclase. See Figure 6 for additional abbreviations.

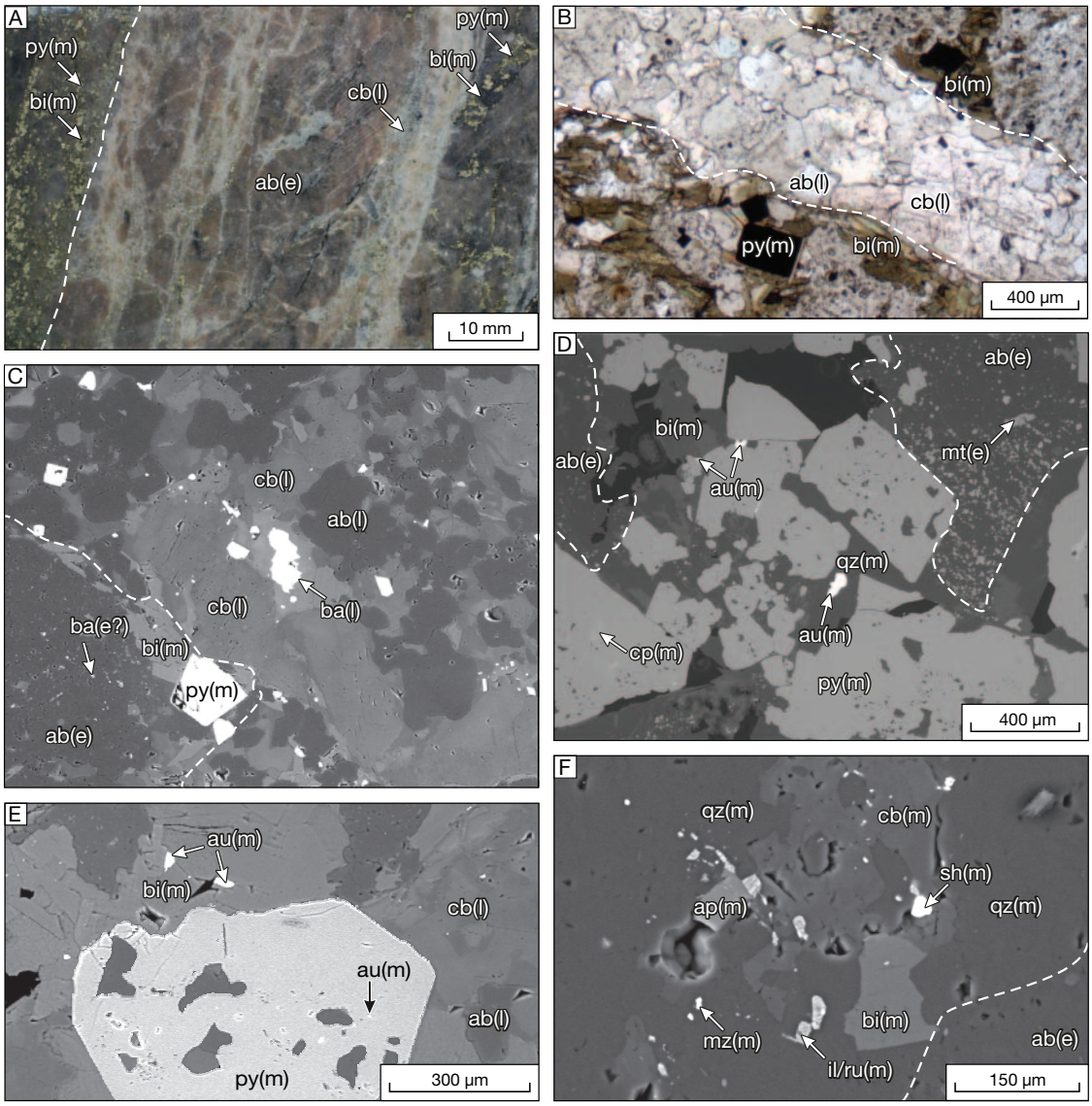

FIG. 8. Common alteration assemblages of the ore domain and mineralized zones of the granotoid domain. A. Albite-biotite-pyrite–altered Devon Consols Basalt (left of the white dashed line) and albite-biotite-pyrite-carbonate–altered granitoid (right of the white dashed line). Devon Consols Basalt and granotoid have been pervasively overprinted by early pervasive albite alteration, which has been crosscut by main-stage biotite-pyrite veins and late-stage carbonate veins (DDH CD7177-260.5m). B. Albite-carbonate-biotite-pyrite–altered Devon Consols Basalt from the lower domain in plane-polarized light. The sample consists of turbid early-stage albite-carbonate alteration that has been crosscut by main-stage biotite-pyrite veins, which in turn have been crosscut by late-stage albite-carbonate veins (DDH CD7055-247.8m). C. Backscattered electron image of late-stage albite-carbonate vein in ore domain Devon Consols Basalt (shown in (B)), showing that the veins consist of abundant barite and pyrite. D. Backscattered electron image of pervasive early-stage albite-magnetite. Early-stage albite-magnetite has been crosscut by main-stage pyrite-quartz-biotite veins which contain gold. Gold occurs as inclusions in quartz and pyrite (DDH CD7176-259.1m). E. Backscattered image of main-stage biotite-pyrite alteration of Devon Consols Basalt from the ore domain (as shown in (B)). Gold inclusions occur in both pyrite and biotite, indicating that main-stage biotite alteration was associated with the deposition of gold in the ore domain. F. Biotite coexisting in a vein with carbonate, apatite, rutile, ilmenite, scheelite monazite, and quartz. The vein crosscuts early albite. Rutile and ilmenite are often intergrown in the ore domain (DDH CD7055-252.0m). See Figure 6 for mineral abbreviations.

(Fig. 10C). These late-stage(?) alteration assemblages can be associated with pentlandite, sphalerite, siegenite, cobaltite, and traces of galena (Fig. 10D-E).

Biotite and Apatite Geochemistry

The composition of biotite and associated apatite across alteration domains of the East Repulse deposit was investigated to determine if geochemical links exist between biotite in the ore domain and biotite in other domains. The composition of biotite and apatite were also used to establish the temperature of biotite-apatite equilibration and to determine the f_{H_2O}/f_{HF} ratios of fluids in equilibrium with biotite (Munoz, 1992; Zhu and Sverjensky, 1992). Since main-stage biotite alteration is associated with gold in the ore and granitoid domains, these

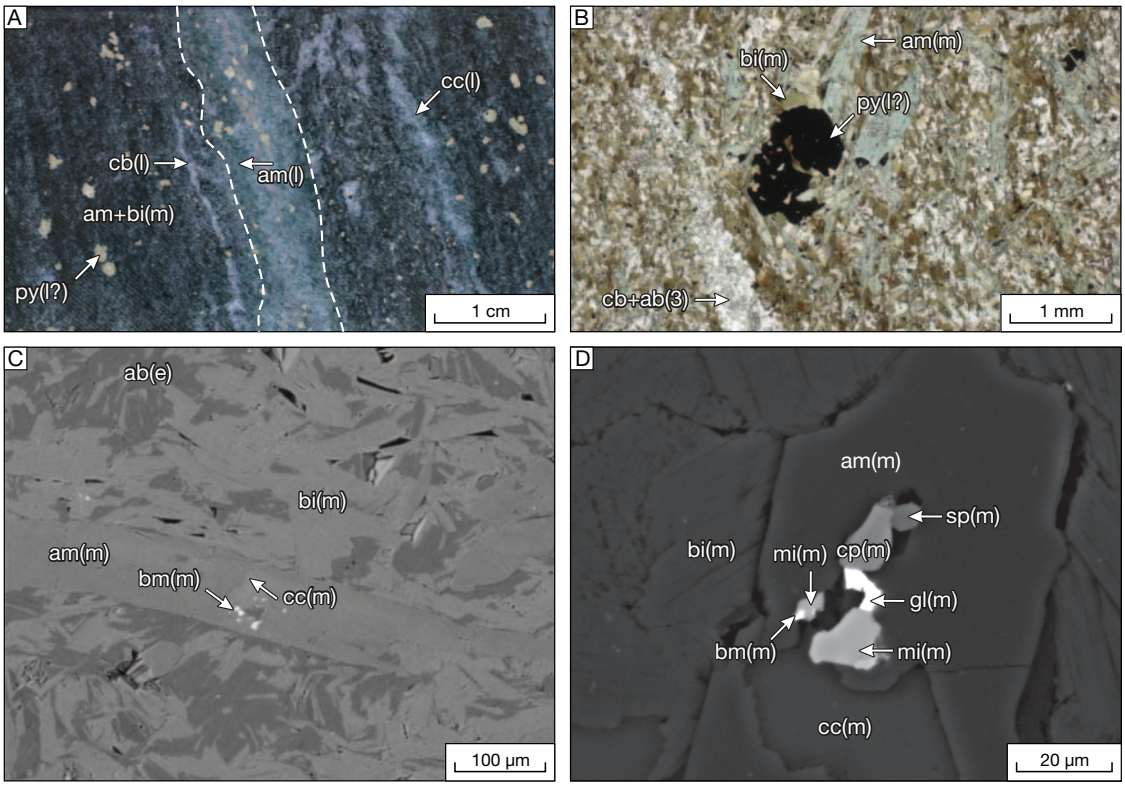

FIG. 9. Transitional domain alteration assemblages. A. Diamond drill core of biotite-amphibole-carbonate-pyrite–altered Paringa Basalt from the transitional domain. Main-stage biotite-amphibole-carbonate alteration has been crosscut by amphibole-carbonate-pyrite veins, which are inferred to be related to late-stage alteration (DDH CD7055-220.7m). B. Transitional domain Paringa Basalt that shows main-stage biotite-amphibole-carbonate alteration in plane-polarized light. Main-stage biotite and amphibole are overgrown by pyrite, which may be related to late-stage alteration. Sample same as (A). C. Backscattered electron image of main-stage amphibole and biotite in Paringa Basalt from the transitional domain (same sample as (A)). Main-stage amphibole contains inclusions of bismuthinite and calcite. D. Backscattered electron image of inclusions in main-stage amphibole from the transitional domain (same sample as (A)). Inclusion includes calcite, bismuthinite, sphene, galena, chalcopyrite, and millerite. See Figure 6 for mineral abbreviations.

temperatures are likely to constrain the temperature of gold mineralization. Analyses were obtained from a range of textural settings and rock types, including main-stage biotite-pyrite veins and stringers in mafic rocks and granitoids of the lower and ore domains and biotitic selvages to anhydrite ± quartz veins in the Devon Consols Basalt in the lower domain. Analyses were also conducted on biotite-apatite pairs from pervasive biotite-amphibole-carbonate–altered zones within Kambalda Komatiite in the lower domain. These pervasive biotite-amphibole-carbonate zones occur around anhydrite ± quartz veins. Biotite-apatite was also analyzed from pervasive biotite-amphibole alteration domains within the transitional domain and on the margins of granitoid intrusions as well as spotty biotite in the upper domain.

Methods

Biotite and apatite grains were mounted in epoxy, polished and coated with carbon prior to analysis. Grains were analyzed using the JEOL 8900R electron probe microanalyzer at the CSIRO laboratories in Clayton, Victoria, Australia. Beam conditions were an accelerating voltage of 15kV, a beam current of 15 nA, and a defocused beam diameter of 10 μm. Elements Si, Ti, Al, Cr, Fe, Mn, Mg, Ca, K, Na, Ba, Cl, and F were analyzed in biotite. Peak counting time for Si, Ti, Al, Fe, Mn, Mg, Ca, K, Cl, and F was 20 s, for Ba 40 s, for Cr 30 s, and for Na 10 s. Background counting times were typically half the peak counting time. The detection limit of halogens in biotite was approximately 560 and 150 ppm for F and chlorine, respectively. Known standards were used at the beginning and end of probe sessions in order to assess accuracy and correct for machine drift during analysis.

All apatite grains analyzed in the current study occur with biotite and are either associated with main-stage alteration or a possible earlier phase of metasomatism and/or metamorphism (e.g., upper-domain Paringa Basalt). Elements Si, Al, Fe, Mn, Mg, Ca, Na, Sr, P, La, Ce, Nd, Eu, Y, S Cl, and F were analyzed in apatite. A peak counting time of 20 s was used for the analysis of Si, Al, Fe, Mn, Mg, Na, Sr, La. Ce, Nd, Eu, Y, and S, whereas a peak counting time of 10 s was used for the analysis of F, P, Cl, and Ca. Background counting times were typically half the peak counting time. Fluorine and Cl had detection limits of between 600 and 660 ppm, respectively. Known standards were also used to assess accuracy and correct for machine drift during probe sessions. Apatite grains that had their *c* axis approximately normal to the beam were preferentially selected for analysis in order to minimize

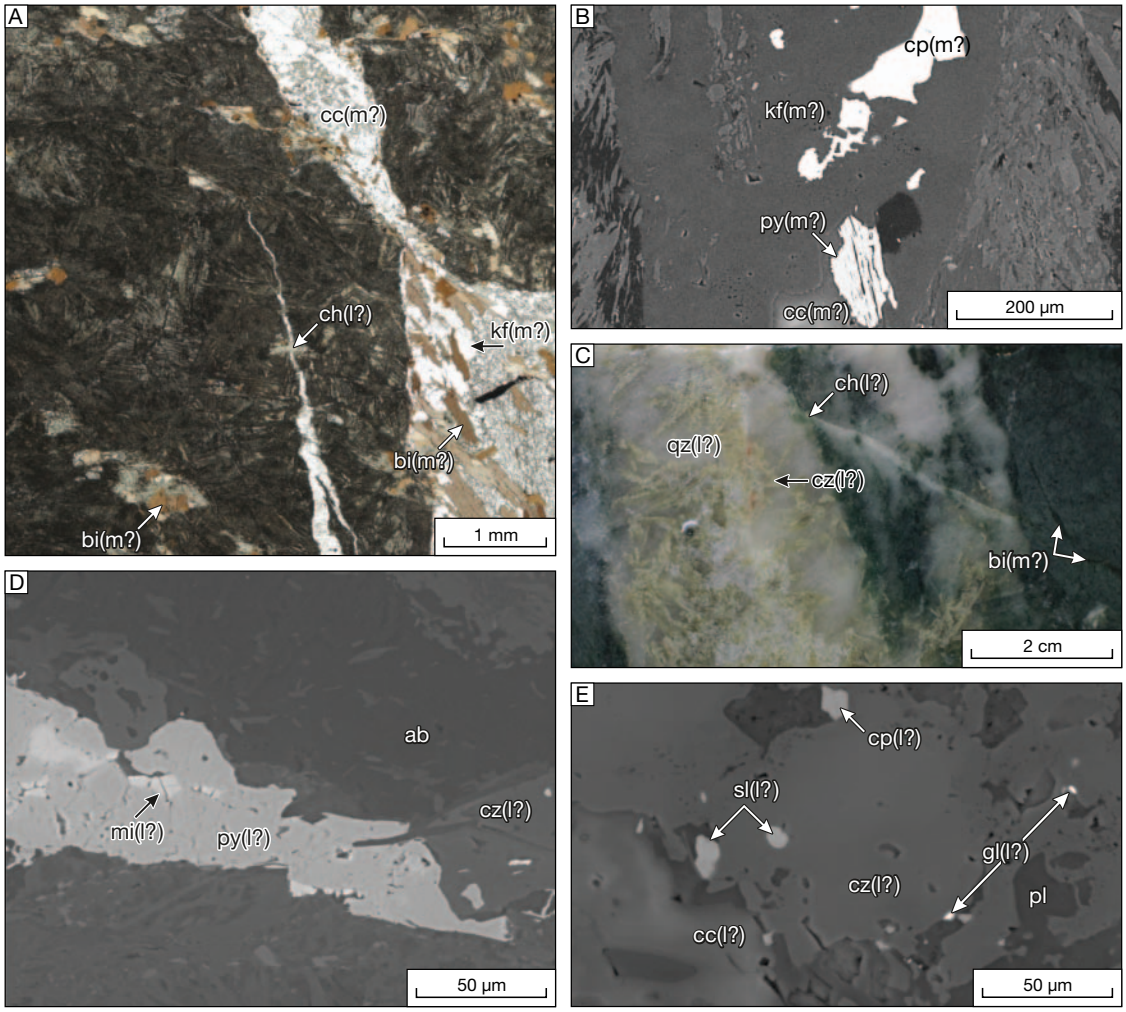

FIG. 10. Alteration assemblages of the upper domain. A. Chlorite-biotite-K-feldspar-calcite–altered Paringa Basalt from the upper domain in plane-polarized light (DDH CD7055-120.8m). The sample includes spotty biotite alteration in the wall rock. The wall rock is also crosscut by calcite-biotite-K-feldspar veins. Spotty biotite has overgrown an earlier phase of chlorite alteration. B. Backscattered electron image of K-feldspar vein with calcite, chalcopyrite, and pyrite from the upper domain (DDH CD7055-89.2m). C. Diamond drill core of quartz-clinozoisite-chlorite-calcite vein, which crosscuts Paringa Basalt from the upper domain. The quartz-clinozoisite-chlorite-calcite vein also crosscuts thin biotite veins (DDH CD7061-63.8m). D. Backscattered electron image of pyrite, millerite, and clinozoisite alteration of Paringa Basalt from the upper domain (same sample as (B)). E. Backscattered electron image of clinozoisite-calcite alteration of Paringa Basalt. Clinoziosite contains inclusions of galena, sphalerite, and chalcopyrite (DDH CD5026-218.4m). See Figure 6 for mineral abbreviations.

the effects of F migration toward the beam (Stormer et al., 1993). In addition the stage was continually moved under the defocused beam, which has been shown to minimize the effect of F migration toward the beam (Webster et al., 2009). Some apatite samples at depths of greater than 300 m have greater than 2 apfu F (equiv to ~3.77 wt %); however it is unclear if this is a result of substitution reactions (see below) and/or the effects of F migration toward the beam. Hence some analyses of apatite may have yielded higher than actual F content.

Estimation of the Fe^{3+}/Fe^{2+} ratio of biotite

Calculation of Fe^{3+}/Fe^{2+} ratios of microprobe analyses of biotite by assuming 14 cations or 24 anions/fu can significantly underestimate the amount of Fe^{3+} (e.g., Feldstein et al., 1996). An alternative approach, in the absence of measured Fe^{2+}, is to approximate Fe^{3+}/Fe_{total} based on the redox conditions of biotite formation indicated by coexisting redox sensitive minerals (Samson et al., 1999). Guidotti and Dyar (1991) reported Fe^{3+}/Fe_{total} values for metamorphic biotite under a range of redox conditions. They reported that biotites in equilibrium with ilmenite and graphite had consistent Fe^{3+}/Fe_{total} of approximately 0.12, biotites coexisting with magnetite had Fe^{3+}/Fe_{total} of 0.22 ± 0.04, and a sample that contained hematite had Fe^{3+}/Fe_{total} values of 0.46 ± 3. Anthony and Titley (1988) used Mössbauer spectroscopy to determine the Fe^{3+}/Fe_{total} of biotites coexisting with quartz, magnetite, and K-feldspar from granodiorite of a porphyry copper deposit in Arizona. Results yielded values between 0.19 and 0.24, which is consistent with values from Guidotti and Dyar (1991) for magnetite-bearing rocks.

In part, biotite from the East Repulse coexists with magnetite, pyrite, quartz, and very minor amounts of K-feldspar

in the hanging wall, core, and footwall of the deposit. Biotite also coexists with ilmenite and rutile in the ore and granitoid domains, anhydrite in the lower domain, and titanite in the upper and lower domains. These assemblages suggest biotite formation over a range of redox conditions, implying a range of Fe^{3+}/Fe_{total} values. However, large inaccuracies in the Fe^{3+}/Fe_{total} ratio (i.e., ±0.1) correspond to relatively small errors in biotite-apatite geothermomtery and $\log(f_{H_2O}/f_{HF})_{fluid}$ calculations (i.e., approximately ±5°C and ±0.02 $\log(f_{H_2O}/f_{HF})_{fluid}$, respectively). Hence for the purpose of reporting biotite analyses here (Table 1) we assume an intermediate value of Fe^{3+}/Fe_{total} of 0.22.

Mg and Ti content of biotite

The Mg number (i.e., $Mg/(Mg + Fe_{total})$) of biotites range between 0.57 and 0.62 in Paringa Basalt from the upper domain (Fig. 11A). In the transitional domain the Mg number of biotite is markedly higher (0.67–0.76) for Paringa Basalt than in the upper domain. Biotite in Devon Consols Basalt, Kapai Slate, and Defiance Dolerite have Mg numbers between 0.66 and 0.78 and overlap with the range of transitional domain biotites. The granitoids also have biotites with a similar range of the Mg number (0.65 and 0.75) in mineralized zones between 220- and 250-m depths. At depths between 300 and 410 m, the granitoids contain biotites with Mg numbers that range between 0.54 and 0.74, which is a greater range than those between 220- and 250-m depths. Biotites in Kambalda Komatiites have Mg numbers between 0.70 and 0.86. Weakly biotite altered Kambalda Komatiite from the hanging wall of the Repulse Thrust in the Leviathan pit (Victory-Defiance deposit; Fig. 1) has biotites with Mg numbers between 0.67 and 0.70.

The Ti in biotite ranges between 0.15 and 0.22 apfu (Fig. 11B) in Paringa Basalt from the upper domain, and between 0.07 and 0.18 apfu for biotite from the transitional-domain Paringa Basalt (Fig. 11B). Devon Consols Basalt contains biotite with between 0.18 and 0.20 apfu Ti, and Defiance Dolerite biotites have between 0.13 and 0.16 apfu Ti. Biotite in granitoids from mineralized zones (220- to 250-m depth) contain between 0.08 and 0.26 apfu Ti. Granitoids that occur at

TABLE 1. Selected Microprobe Analysis of Biotite from the East Repulse Deposit

Rock unit	Paringa Basalt		Defiance Dolerite	Devon Consol Basalt		Granitoid		Kambalda Komatiite	
DDH	CD7055	CD7055	CD7177	CD7177	CD7055	CD7177	CD7055	CD7177	CD7055
Depth	150.6	220.0	282.2	228.0	294.8	253.2	399.9	372.0	440.8
SiO_2	37.19	38.35	39.61	39.62	37.98	39.09	38.71	38.06	38.89
TiO_2	2.00	1.28	1.19	1.49	1.23	1.58	1.58	0.85	0.66
Al_2O_3	17.21	14.64	13.75	14.26	16.08	15.27	15.27	15.87	14.20
FeO	15.72	11.28	11.81	10.19	13.98	14.33	13.48	13.02	9.15
MnO	<0.12	0.20	<0.12	0.16	0.24	<0.12	<0.12	0.15	<0.12
MgO	14.48	20.08	18.17	19.09	17.42	13.97	19.30	17.25	21.20
Na_2O	0.08	0.11	0.11	0.09	0.05	0.08	0.05	0.11	0.28
K_2O	10.22	10.73	10.50	10.36	10.40	10.32	10.51	10.36	10.63
BaO	0.45	<0.04	0.12	0.05	0.10	0.25	0.59	0.06	<0.04
Cr_2O_3	0.31	0.34	0.31	<0.15	<0.15	0.00	<0.15	0.37	0.25
CaO	0.28	<0.03	0.04	<0.03	<0.03	0.05	<0.03	0.10	<0.03
Cl	0.017	0.028	<0.015	0.020	0.020	<0.015	<0.015	<0.015	0.015
F	0.19	0.36	0.70	0.19	0.62	0.35	1.51	0.42	0.50
Total	98.24	97.39	96.58	95.60	98.23	95.42	101.02	96.70	95.90
-O = F	0.08	0.15	0.29	0.08	0.26	0.15	0.64	0.18	0.21
Total	98.16	97.24	96.28	95.52	97.96	95.27	100.38	96.53	95.69
Calculated by normalizing to 20 O + 4 (OH, F, Cl)									
Si	5.400	5.535	5.786	5.754	5.489	5.790	5.492	5.558	5.651
Al(IV)	2.600	2.465	2.214	2.246	2.511	2.210	2.508	2.442	2.349
Al(VI)	0.345	0.026	0.153	0.195	0.228	0.456	0.043	0.289	0.083
Ti	0.218	0.139	0.130	0.163	0.134	0.177	0.168	0.093	0.072
Fe^{3+A}	0.420	0.299	0.317	0.272	0.372	0.390	0.352	0.350	0.245
Fe^{2+A}	1.489	1.061	1.125	0.965	1.318	1.384	1.247	1.240	0.868
Mg	3.134	4.320	3.956	4.134	3.752	3.085	4.081	3.755	4.592
Mn	0.013	0.024	-	0.020	0.029	-	-	0.018	0.011
Ca	0.043	-	0.006	-	-	0.007	-	0.015	-
Na	0.024	0.030	0.031	0.027	0.013	0.024	0.012	0.031	0.078
K	1.894	1.975	1.956	1.920	1.916	1.950	1.902	1.930	1.969
OH	3.908	3.828	3.676	3.909	3.690	3.835	3.349	3.807	3.576
F	0.087	0.165	0.324	0.086	0.305	0.165	0.651	0.193	0.421
Cl	0.004	0.007	-	0.005	0.005	-	-	-	0.004

Notes: Note that detection limits (e.g., <0.1) are approximate values for the analysis; $^{A}Fe^{3+}/Fe_{total}$ values are fixed at 0.22

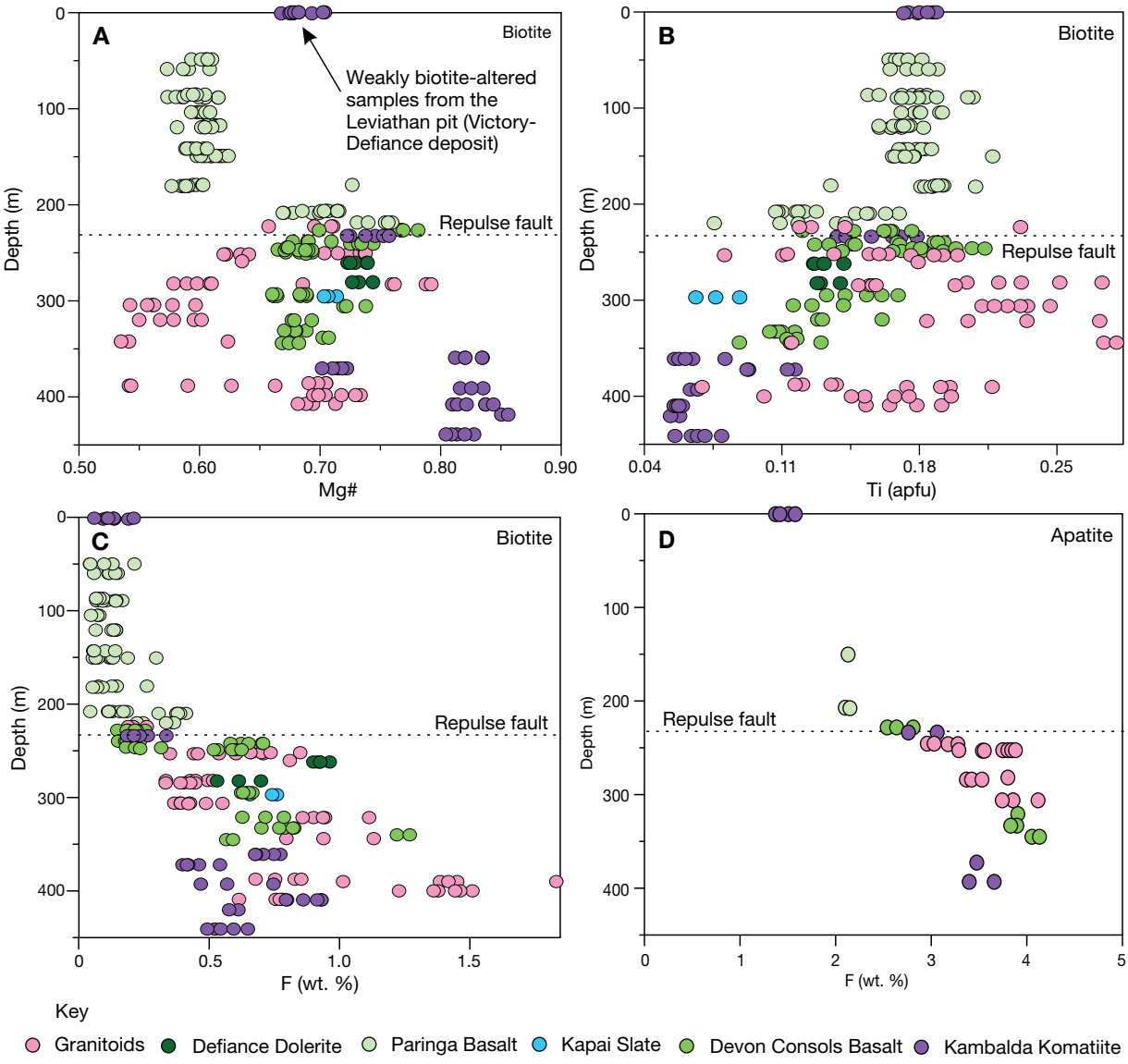

FIG. 11. Element and element ratios of biotite and apatite versus depth (samples collected from DDH CD7055, CD7061 and CD7177). A. Biotites from the upper domain (i.e. <200-m depth) and some granitoids have the lowest Mg number. Ore and transitional domain biotites and some granitoids have intermediate Mg numbers, whereas biotite from the Kambalda Komatiite has the highest Mg number. B. The Ti value of biotites shows almost the opposite trend to Mg number, and hence upper domain biotites and some granitoids have the highest Ti values. Biotites from the ore and transitional domains and some granitoid have intermediate Ti values, whereas biotite from Kambalda Komatiite has the lowest values. C. Fluorine in biotite vs. depth for different rock units across the East Repulse deposit. There is an increase in the amount of F with depth for biotites that occur in basalts and granitoids. Biotites in Kambalda Komatiite are variably enriched in F, which does not appear to correlate with depth. D. The distribution of F in apatite with increasing depth for the East Repulse deposit. There is an increase in F in apatite with increasing depth. The main trend of increasing F in apatite with increasing depth mirrors the trend of F in biotite.

depths of between 300 and 400 m have biotites with between 0.07 and 0.32 apfu Ti. Kambalda Komatiite and Kapai Slate have biotites with the lowest abundance of Ti, which is between 0.05 and 0.10 apfu. Biotites from weakly biotite altered Kambalda Komatiite from the hanging wall of the Repulse Thrust in the Leviathan pit (Victory-Defiance deposit) have between 0.16 and 0.21 apfu Ti. There is a general decrease in the amount of Ti in biotites with depth in Paringa Basalt and Kambalda Komatiite but a general increase in the Mg number.

Halogens in biotite

The abundance of F in biotite is lowest in the Paringa Basalt from the upper domain (<0.06–0.30 wt % or <0.03–0.14 apfu) and most elevated in the biotites from the granitoid intrusions that occur in the deepest parts of the studied cross section (i.e., 0.9–1.8 wt % or 0.43–0.85 apfu; Fig. 11C; Table 1). Biotite from Paringa Basalt of the transitional domain contains between 0.25 to 0.4 wt % F (0.12–0.19 apfu), and the ore domain biotite from Devon Consols Basalt, Defiance Dolerite, Kapai Slate, and granitoid intrusions contain between

0.5 and 1 wt % F (0.24–0.47 apfu). Biotite from Devon Consols Basalt of the lower domain occurs as selvages to quartz-anhydrite veins (Fig. 6F, G) and has between 0.7 and 1.3 wt % F (0.33–0.61 apfu). Kambalda Komatiite biotites contain the lowest abundance of F (0.5–0.9 wt % or 0.24–0.43 apfu) for rocks in the lower domain. Biotite from weakly biotite altered Kambalda Komatiite from the Leviathan pit has F between 0.05 and 0.21 wt % and is within the range of Paringa Basalt from the hanging wall of the East Repulse deposit. Chlorine in biotite is mostly below detection limit (150 ppm) for all rock types; however some individual analyses yielded values as high 350 ppm.

Halogens in apatite

The abundance of F is lowest in apatite from the upper domain Paringa Basalt (2.1–2.3 wt % or 1.12–1.22 apfu; Fig. 11D; Table 2), and the abundance of F in apatite increases from the upper to the lower domain (2.1–4.1 wt % or 1.12–2.18 apfu). In particular, F is highest in apatites from granitoid intrusions and Devon Consols Basalt, which occur at depths greater than 300 m (3.7–4.1 wt % or 1.97–2.18 apfu). These apatites are mostly stoichiometrically enriched in F relative to the normal 2 apfu (equiv to ~3.77 wt %), which may indicate some substitution of $(CO_3^{2-}F^-)$ for PO_4^{3-} in the structure (Binder and Troll, 1989) and/or analytical error. The total abundance of P, S, and Si is between 5.8 and 6.0 apfu, indicating that $(CO_3^{2-}F^-)$ substitution may have occurred in some samples, but is limited (i.e., <0.2 apfu or <0.4 wt % F). Apatite from weakly biotite altered Kambalda Komatiite from the Leviathan pit has a relatively low abundance of the F (i.e., 1.8–2 wt %). The trend of increasing F in apatite with increasing depth parallels the increase in F in biotite with increasing depth.

Biotite-apatite geothermometry

The biotite-apatite geothermometer of Zhu and Sverjensky (1992) was used to estimate the temperature at which apatite and biotite pairs equilibrated. This geothermometer is less prone to subsolidus reequilibration compared to carbonates and oxides (Tacker and Stormer, 1989; Andersen and Austrheim, 1991). Apatite is also considered to be less vulnerable than micas to subsolidus exchange of halogens (Parry and Jacobs, 1975; Tracker and Stormer, 1989; Piccoli and Candela, 1994). Apatite and biotite grains selected for analysis were in direct contact and are from main-stage veins in the ore domain (Fig. 12A). For samples used in the current study, apatite occurs as euhdral to subhedral inclusions in biotite grains with no obvious textural evidence for disequilibrium

TABLE 2. Selected Microprobe Analysis of Apatite from the East Repulse Deposit

Rock unit	Paringa Basalt		Devon Consol Basalt		Granitoids			Kambalda Komatiite	
DDH	CD7061	CD7177	CD7177	CD7061	CD7177	CD7177	CD7177	CD7177	CD7177
Depth	150.7	208.0	228.0	344.4	253.2	284.4	306.0	372.0	392.8
SiO_2	0.22	0.04	0.10	0.07	0.04	0.20	0.09	0.11	0.08
La_2O_3	<0.2	<0.2	<0.2	<0.2	<0.2	<0.2	<0.2	<0.2	<0.2
Ce_2O_3	0.11	0.10	<0.08	<0.08	<0.08	<0.08	<0.08	<0.08	<0.08
Nd_2O_3	<0.07	<0.07	<0.07	<0.07	<0.07	0.09	0.07	<0.07	<0.07
Eu_2O_3	<0.07	<0.07	<0.07	<0.07	<0.07	<0.07	<0.07	<0.07	<0.07
Y_2O_3	<0.18	<0.18	<0.18	<0.18	<0.18	<0.18	<0.18	<0.18	0.19
Fe_2O_3	0.34	0.75	0.17	0.11	<0.1	<0.1	0.17	0.15	0.25
MnO	<0.1	<0.1	<0.1	<0.1	<0.1	<0.1	<0.1	<0.1	<0.1
MgO	<0.4	<0.4	<0.4	<0.4	<0.4	<0.4	<0.4	<0.4	<0.4
CaO	55.58	55.02	55.01	55.47	55.72	54.84	55.70	55.04	55.10
SrO	<0.11	0.12	0.55	<0.11	0.18	0.31	<0.11	<0.11	<0.11
NaO	<0.05	0.14	0.09	<0.05	0.14	0.16	0.12	<0.05	0.07
K_2O	<0.05	<0.05	<0.05	<0.05	<0.05	<0.05	<0.05	<0.05	<0.05
P_2O_5	41.78	41.99	42.22	42.28	42.07	41.16	41.85	42.22	41.97
SO_3	<0.22	<0.22	<0.22	<0.22	<0.22	0.31	<0.22	<0.22	<0.22
F	2.13	2.12	2.80	4.05	3.56	3.36	3.86	3.47	3.66
Cl	<0.07	<0.07	<0.07	<0.07	<0.07	<0.07	<0.07	<0.07	<0.07
Total	100.17	100.28	100.92	101.98	101.70	100.43	101.84	101.00	101.31
-O = F, Cl	0.90	0.89	1.18	1.71	1.50	1.42	1.62	1.46	1.54
Total	99.27	99.39	99.74	100.27	100.21	99.01	100.22	99.53	99.77
Number of ions on the basis on 16 cations									
Si	0.04	0.01	0.02	0.01	0.01	0.03	0.01	0.02	0.01
Fe	0.05	0.11	0.02	0.02	-	-	0.02	0.02	0.03
Ca	9.98	9.87	9.88	9.97	9.98	9.94	9.99	9.94	9.93
Sr	-	0.01	0.05	0.00	0.02	0.03	0.00	-	0.00
Na	-	0.04	0.03	-	0.05	0.05	0.04	-	0.02
P	5.93	5.95	5.99	6.00	5.95	5.90	5.93	6.02	5.98
S	-	-	-	-	-	0.04	-	-	-
F	1.13	1.12	1.49	2.14	1.88	1.80	2.04	1.85	1.95
Cl	-	-	-	-	-	-	-	-	-
OH	0.87	0.88	0.51	-	0.12	0.20	-	0.15	0.05

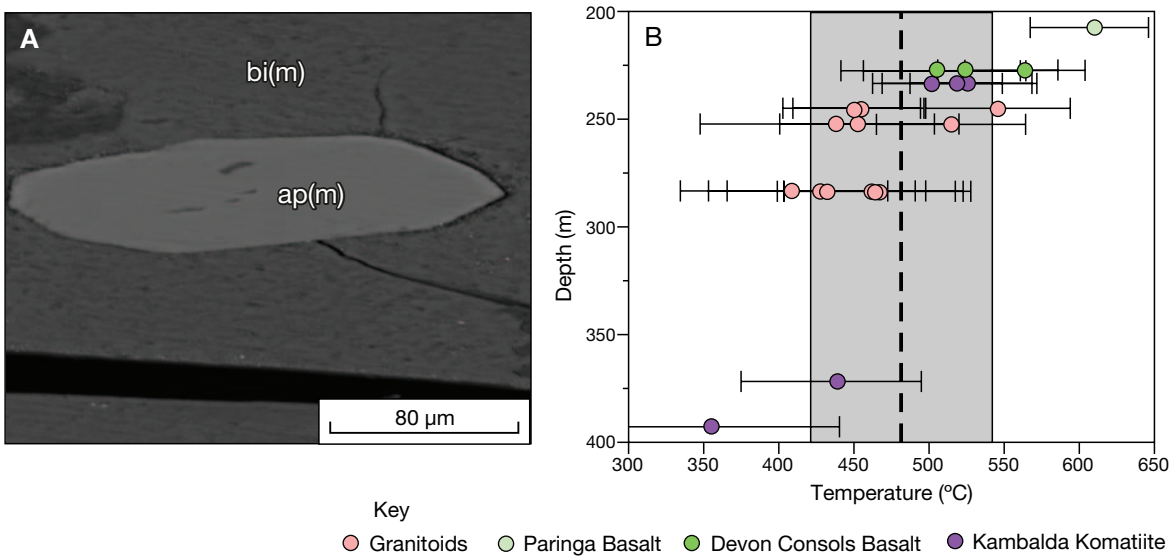

FIG. 12. A. Apatite and biotite, like this example, were selected for electron microprobe analysis and geothermometry estimates. These two phases appear to be in equilibrium. B. Depth vs. calculated temperature from biotite-apatite geothermometry. The graph demonstrates that there is a tendency for lower calculated temperatures with increasing depth. It is unclear if this trend truly reflects a temperature gradient, or is it an effect of the substitution of $(CO_3^{2-}F^-)$ for PO_4^{3-}, resulting in lower calculated temperatures with increasing depth. Dash line represents average temperature and gray area represents 1σ of uncertainty.

between the two phases. Temperature estimates are based on electron microprobe data (Table 3). The formula used to calculate temperatures is the following:

$$T\ (°C) = ((8852 - 0.024\ P\ (bars) + 5000X_{Fe}^{Bi})/(1.987\ \ln K_d^{Ap/Bi} + 3.3666)) - 273.15, \quad (1)$$

where

$$X_{Fe}^{Bi} = (Fe^{2+} + Al^{[VI]})/(Fe^{2+} + Mg + Al^{[VI]}), \quad (2)$$

and

$$K_d^{Ap/Bi} = (X_F/X_{OH})^{Ap}/(X_F/X_{OH})^{Bi}, \quad (3)$$

and X_F and X_{OH} are mole fractions of F and OH in apatite and biotite.

The effects of pressure are negligible (i.e., 2 ± 1 kbars corresponds to temperature variations of less than ±5°C), and the analytical error associated with F analysis is the largest source of uncertainty in calculating temperatures. A pressure of 2 kbars was assumed here, which is based on estimates of mineral equilibria and fluid inclusions of the nearby Victory deposit (Clark et al., 1989).

Temperature estimates were made for 21 biotite-apatite pairs. Most pairs were from a limited depth interval between 225 and 290 m within the transitional and ore domains and were selected from diamond drill holes CD7061 and CD7177 (Fig. 2B). As mentioned above, apatite samples from areas of the lower and granitoid domains have measured F values of greater than 2 apfu and may contain some CO_3^{2-} ions (Binder and Troll, 1989). Hence their true composition could not be determined and therefore they were not used for geothermometry. For the purpose of the calculations, it is assumed that apatites, which have less than 2 apfu F, have negligible amounts of CO_3^{2-} in their structure, although this may not always be the case. In any case, an overestimate of the abundance of F in the hydroxyl site of apatite, through the substitution of $(CO_3^{2-}F^-)$ for PO_4^{3-} or analytical error, would result in lower calculated temperatures. For example a 10% overestimation of F in the hydroxyl site of apatite would yield calculated temperatures that are approximately 40°C cooler. Hence temperature estimates provided here may be considered minimum temperature estimates.

Biotite-apatite pairs from Devon Consols Basalt and granitoid intrusions yielded temperatures between 410° and 560°C (Fig. 12B). Biotite-apatite pairs from Kambalda Komatiite in the lower domain showed a wide range in calculated temperature (360°–440°C). Temperature estimates within the lower domain are within error of estimates within the ore domain, and therefore no thermal gradient can be established from the current dataset.

The average temperature for apatite-biotite pairs is approximately 480°C with a standard deviation of 60°C. The average temperature is higher than some previous temperature estimates, although within error of gold deposition in the Victory-Defiance complex (390° ± 40°C for carbonates; Clark et al., 1989). Early and late alteration assemblages that comprise of epidote-quartz-carbonate in mafic rocks and albite-carbonate in granitoids may reflect relatively low temperature alteration assemblages (i.e., <400°C, Dilles and Einaudi, 1992). However as shown by Bird and Helgeson (1980, 1981) epidote can be stable at temperatures above 600°C.

Halogen fugacity of fluids

The concentration of F and Cl in hydrothermal biotite reflects the F and Cl content of the fluid, expressed as fugacity

TABLE 3. Apatite-Biotite Geothermometry

DDH	Depth	Host rock	Analysis no.	F^{Bi} (wt %)	F^{Ap} (wt %)	X_F/XOH_{AP}	X_F/X_{OH}^{Bi}	$\ln K_D$	X_{Fe}^{Bi}	T (°C)	+ve error[1]	-ve error[1]
CD7177	208.0	Paringa Basalt	26b	0.19	2.12	1.26	0.020	4.12	0.282	607	40	–43
CD7177	228.0	Devon Consols Basalt	39b	0.19	2.54	2.12	0.022	4.56	0.219	522	60	–67
CD7177	228.0	Devon Consols Basalt	37b	0.13	2.80	2.90	0.029	4.61	0.328	561	39	–40
CD7177	228.0	Devon Consols Basalt	36c	0.19	2.64	2.29	0.022	4.64	0.198	504	54	–63
CD7061	233.9	Kambalda Komatiite	143a	0.34	3.06	4.48	0.041	4.67	0.247	518	49	–50
CD7061	233.9	Kambalda Komatiite	143b	0.19	2.76	2.74	0.022	4.82	0.246	502	45	–41
CD7061	233.9	Kambalda Komatiite	145a	0.21	2.76	2.69	0.025	4.67	0.262	526	44	–40
CD7061	246.0	Granitoid	136a	0.32	3.28	6.53	0.027	5.47	0.315	454	41	–44
CD7061	246.0	Granitoid	137b	0.32	3.03	4.22	0.039	4.68	0.312	545	47	–48
CD7061	246.0	Granitoid	140a	0.19	3.17	5.66	0.022	5.55	0.303	449	44	–46
CD7177	253.2	Granitoid	46c	0.35	3.56	15.08	0.043	5.82	0.374	438	65	–90
CD7177	253.2	Granitoid	46d	0.35	3.30	7.07	0.043	5.10	0.374	517	47	–49
CD7177	253.2	Granitoid	50c	0.54	3.53	15.01	0.051	5.68	0.362	455	57	–70
CD7177	284.4	Granitoid	59c	0.54	3.54	15.45	0.040	5.96	0.311	408	56	–68
CD7177	284.4	Granitoid	59b	0.54	3.36	8.70	0.040	5.35	0.311	464	57	–64
CD7177	284.4	Granitoid	58c	0.39	3.42	10.27	0.047	5.33	0.225	433	57	–67
CD7177	284.4	Granitoid	58b	0.43	3.40	14.50	0.051	5.14	0.259	468	58	–65
CD7177	284.4	Granitoid	57a	0.41	3.37	8.14	0.048	5.11	0.232	461	54	–61
CD7177	284.4	Granitoid	56c	0.45	3.42	8.92	0.054	5.58	0.274	428	68	–92
CD7177	372.0	Kambalda Komatiite	85a	0.42	3.47	13.18	0.051	5.55	0.289	439	54	–63
CD7177	392.8	Kambalda Komatiite	89b	0.47	3.66	37.94	0.094	6.00	0.163	356	84	–[2]

[1] Errors are based on analytical error (2) for apatite and biotite microprobe analysis; typical fluorine analytical error is 10 to 15% for biotite and 3 to 4% for apatite; analytical error for iron, magnesium, silicon, aluminum, and titanium in biotite is less than 3.5 %

[2] Minimum temperature constraint not obtained due to fluorine in apatite being >2 apfu when analytical error is accounted for

Note pressure has been fixed to 2,000 bars

ratios f_{H_2O}/f_{HF}, f_{H_2O}/f_{HCl} and f_{HF}/f_{HCl}, as well as fluid temperature. The fugacity ratio may be determined from the following equations that have been derived from experimental and thermodynamic data (Munoz, 1992) as follows:

$$\log(f_{H_2O}/f_{HF})_{fluid} = 1{,}000/T[2.37 + 1.1(X_{Mg})_{biotite}] + 0.43 - \log(X_F/X_{OH})_{biotite}, \quad (4)$$

$$\log(f_{H_2O}/f_{HF})_{fluid} = 1{,}000/T[1.15 - 0.55(X_{Mg})_{biotite}] + 0.68 - \log(X_{Cl}/X_{OH})_{biotite}, \quad (5)$$

$$\log(f_{HF}/f_{HCl})_{fluid} = 1{,}000/T[1.22 + 1.65\ (X_{Mg})_{biotite}] + 0.25 + \log(X_F/X_{Cl})_{biotite}, \quad (6)$$

where T is the temperature in Kelvin of the halogen exchange, X_{Mg} is the mole fraction of Mg in the octahedral site, and X_F and X_{OH} are mole fractions of F and hydroxyl in the hydroxyl site of the biotite. We have used a temperature of halogen exchange of 480°C from the biotite-apatite geothermometry to calculate the fugacity ratios f_{HF}/f_{HCl}, f_{H_2O}/f_{HCl}, and f_{HF}/f_{HCl}. Analytical challenges associated with apatite tend to yield higher than actual F values, which will result in lower temperature estimates. A slight error and/or bias in the temperature estimate from apatite-biotite will affect the H_2O/HF and H_2O/HCl activity ratios but the relative changes of these ratios from below to above the ore zone will not change.

$\text{Log}(f_{H_2O}/f_{HF})_{fluid}$ values are between 5.1 and 5.4 for Devon Consols Basalt from the lower domain (Fig. 13A). Calculated fluids in equilibrium with biotite in granitoid intrusions have $\log(f_{H_2O}/f_{HF})_{fluid}$ values of approximately 5.8 at depths of 225 m but decreases to values of approximately 5.0 at depths of 390 m. Kambalda Komatiite at depths of between 350 and 450 m has higher $\log(f_{H_2O}/f_{HF})_{fluid}$ for fluids in equilibrium with biotite compared to other rock types at similar depths (5.4–5.75). Biotite in these samples may have equilibrated with earlier metasomatic and/or metamorphic fluids. Fluids in equilibrium with biotite from Devon Consols Basalt, Defiance Dolerite, and Kapai Slate ore domain have values between 5.2 and 6.1 and also show decreasing values with increasing depth. Fluids in equilibrium with biotite from Paringa Basalt in the upper and transitional domains are calculated to have $\log(f_{H_2O}/f_{HF})_{fluid}$ values between 5.6 and 6.3 (Fig. 13A). Our calculated $\log(f_{H_2O}/f_{HF})_{fluid}$ values are also shown in Figure 13B, as a function of biotite composition. Figure 13B shows isolines of biotites formed at a range of fluid composition over a constant temperature, following Zhu and Sverjensky (1992) and indicates that $\log(f_{H_2O}/f_{HF})_{fluid}$ varies independently of rock type.

Similarly, there appears to be no significant difference between biotite from different rock types and alteration domains on the $\log(X_{Cl}/X_{OH})$ versus X_{Mg} (Fig. 13C). Fluids in equilibrium with biotite had $\log(f_{H_2O}/f_{HCl})_{fluid}$ between 5.0 and 5.7; although higher values are likely given that chlorine analyses that were below the detection limit have been excluded. $\text{Log}(f_{HF}/f_{HCl})_{fluid}$ ranged from –0.16 to –1.88, and the ratio was close to unity with highest f_{HF} relative to f_{H_2O}. However higher $\log(f_{HF}/f_{HCl})_{fluid}$ values are likely given that most biotites had less than 150 ppm Cl and were not used in fugacity calculations here.

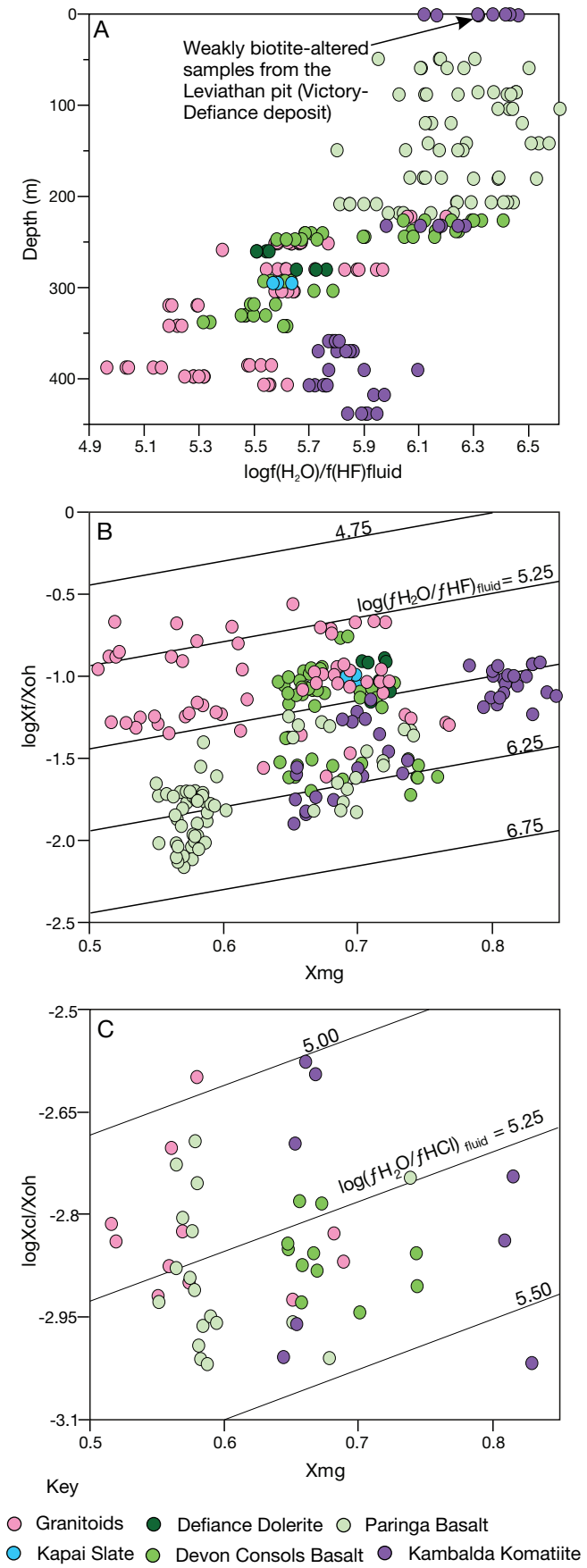

Whole-Rock Geochemistry

Samples

X-ray fluorescence (XRF) K data for metabasalts and metakomatiites from the East Repulse deposit were used to assess K alteration. Biotite is the main K-bearing phase across the East Repulse deposit, and therefore whole-rock K is used here as a proxy for biotite alteration. Granitoids were also analyzed; however these rocks contain primary K-feldspar phenocrysts, and hence K values do not strictly reflect biotite alteration.

Ion-selective electrode (ISE) and XRF analysis of F was conducted in order to test for host-rock F enrichment of variably altered samples. Samples used were from each of the five main alteration domains and correspond to samples used for biotite and apatite analysis.

Methods

Whole-rock samples were crushed using a steel jaw crusher and small chips (3–15 mm) were then separated and washed in an ultrasonic cleaner for 10 min. Clean chips were then dried and milled using agate or mild steel mills. Mills were cleaned using quartz sand and thoroughly scrubbed with synthetic cleaning pads in hot soapy water, rinsed, and then dried using compressed air between samples to reduce chances of contamination.

X-Ray Whole-Rock Analysis (K and F)

XRF analysis of K and F was conducted at the University of Tasmania. Fusion disks (32 mm) were made with a 1:9 dilution of sample: 12-22 flux (12 pts. $Li_2B_4O_7$-22 pts. $LiBO_2$), fused for 10 to 15 min at 1,100°C in a 5% Au/Pt crucible, and poured into a 5% Au/Pt mould. These were used for major element analysis including K and F. For F, standard disks (0, 2.5, 5.0, 10.0 wt % F in SiO_2) were prepared with ignited CaF_2 and pure quartz. Fusion disks of 25 international reference rocks containing 0.001 to 8.62 wt % F were prepared to check the accuracy of the method. A PANalytical Axios Advanced XRF Spectrometer with SST-mAX 4kW Rh tube was operated at 25kV 160 mA, using a PX-1 multilayer, vacuum, 700 μmm collimator, flow counter with P10 gas, K alpha (FKA) with backgrounds of –3.39° and +2.11° to avoid Fe and Al lines. A correction was made for the FeLA overlap. Counting times of 200, 200, 200 s (bgd.1, peak, bgd.2) gave a detection limit (3σ) of 0.04 wt % F. Samples were analyzed in duplicate (Table 4). Table 4 compares the XRF results with published values for the reference rocks. Note that many published values are not certified as F is not an easy element to determine and there is often poor agreement between laboratories.

FIG. 13. A. Depth vs. calculated HF fugacity ratios of fluids in equilibrium with biotite (at 480°C) from the East Repulse deposit. The log (f_{H_2O}/f_{HF}) for fluids in equilibrium with biotite decreases with increasing depth in granitoids and biotite-anhydrite–altered basalt, which may reflect a decrease in the activity of HF in fluids as they moved through the wall rocks from depth. B. X_{Mg} vs. log (X_F/X_{OH}) for biotite from each of the lithologies of the East Repulse deposit. Parallel lines show log (f_{H_2O}/f_{HF}) values of fluids in equilibrium with biotite at 480°C (see text). C. X_{Mg} vs. log (X_{Cl}/X_{OH}) for biotite from each of the alteration domains of the East Repulse deposit. Parallel lines show log (f_{H_2O}/f_{HF}) values of fluids in equilibrium with biotite at 480°C.

TABLE 4. Rock Reference Materials and Selected Unknowns from ISE and XRF Whole-Rock Analysis of Fluorine

Method			XRF			ISE		Published	
Detection limit			0.04	sd	Duplicate	0.01	Duplicate	values	sd
Reference material	Depth	Rock unit	(wt %)	(wt %)	(wt %)	(wt %)	(wt %)	(wt %)	(wt %)
GBW 07113						0.130		0.130	
SCO-1						0.080		0.080	
DR-N						0.050		0.050	
UB-N						<0.01		0.010	
W-2a						0.010		0.021	
SGR-1b						0.200		0.196	
BHVO-2 (6x)			0.040	0.032				0.040	
JG-1			0.055					0.050	
JR-1 (3x)			0.089	0.025				0.094	
AC-E (3x)			0.214	0.019				0.210	
GSP-2 (3x)			0.385	0.022				0.30 to 0.41	
OShBO (5x)			1.190	0.070				1.130	0.160
MICA-FE			1.660					1.600	
MA-N (4x)			1.455	0.024				1.3 to 1.7	
MICA-MG (10x)			2.790	0.060				2.850	
GXR3/538			8.640					8.620	0.340
Selected unknowns from the East Repulse deposit									
Diamond drill hole	Depth	Rock unit	XRF		Duplicate	ISE	Duplicate		
CD7055	60.1	Paringa Basalt	<0.04		<0.04	<0.01			
CD7055	180.8	Paringa Basalt	<0.04		<0.04	<0.01			
CD7055	326.45	Devon Consol Basalt	0.170		0.166	0.130			
CD7055	360.9	Kambalda Komatiite	0.060		0.040	0.040			
CD7055	409.6	Kambalda Komatiite	0.397		0.401	0.420			
CD7055	440.8	Kambalda Komatiite	0.250		0.246	0.310			
CD7177	253.2	Granitoid				<0.01	<0.01		
CD7055	290.25	Devon Consol Basalt				0.150	0.170		

Ion-Selective Electrode F Analysis

Ion-selective electrode analysis for F in whole rock was conducted by Activation Laboratories Limited, Ontario, Canada. For the analyses, 0.2 g of samples were fused with a combination of lithium metaborate and lithium tetraborate in an induction furnace. The fuseate was dissolved in dilute nitric acid, and the ionic strength was adjusted using an ammonium citrate buffer. The fluoride ion electrode is immersed in this solution to measure the fluoride-ion activity directly. An automated Mandel Scientific fluoride analyzer was used for the analysis. Certified standards were used throughout the analysis (Table 4). Comparison between ISE and XRF results shows that most analyses are within 20% of each other (Table 4).

Results

Paringa Basalt in the hanging wall has between 0.03 and 0.7 wt % K_2O (Fig. 14A). In the transitional domain, where biotite-amphibole alteration is pervasive, the Paringa Basalt has between 3 and 5 wt % K_2O, indicating that these rocks contain greater than four times the amount of K compared to their least altered equivalent. Devon Consols Basalt in the ore domain has between 1.2 and 3 wt % K_2O, whereas in the lower domain it has a wider range between 0.2 and 4.6 wt % K_2O. The wide range of K_2O in the lower domain reflects variable degrees of biotite alteration throughout the ore and lower domains. A talc-chlorite-carbonate–altered Kambalda Komatiite sample from the transitional domain contains 0.1 wt % K_2O, and least biotite altered Kambalda Komatiite rocks from the Leviathan Pit contain <0.22 wt % K_2O. Kambalda Komatiite in the lower domain show pervasive biotite-amphibole-carbonate alteration and contains between 4.5 and 5 wt % K_2O.

Whole-rock F values were plotted against depth (Fig. 14B). Results show that upper domain Paringa Basalts have F values of less than 0.01 wt %. The talc-chlorite-carbonate–altered Kambalda Komatiite from the transitional domain contains 0.04 wt % F. Variably biotite altered Devon Consols Basalt from the ore and lower domain contains 0.09 to 0.33 wt % F, and biotite-amphibole–altered Kambalda Komatiites from the lower domain contain between 0.25 and 0.50 wt % F. Overall there appears to be an increase in the amount of F in mafic and ultramafic rock types with increasing depth.

Most granitoids from the ore and lower domain contain less than 0.01 wt % F; although two samples contain 0.10 and 0.13 wt % F. These two samples are from the lower domain area and appear to contain more biotite than other samples. Two granitoid samples from the ore domain contain 0.01 and 0.02 wt % F, respectively.

Fluorine versus K shows that Kambalda Komatiites from the lower domain have the highest abundance of F and K (Fig. 14C). Biotite-rich Devon Consols Basalts from the lower and ore domains have highly variable F/K ratios, which likely reflects (1) increases in the F content of biotite and apatite with increasing depth and (2) the possibility that other phases such as amphibole, titanite, and/or epidote contain F.

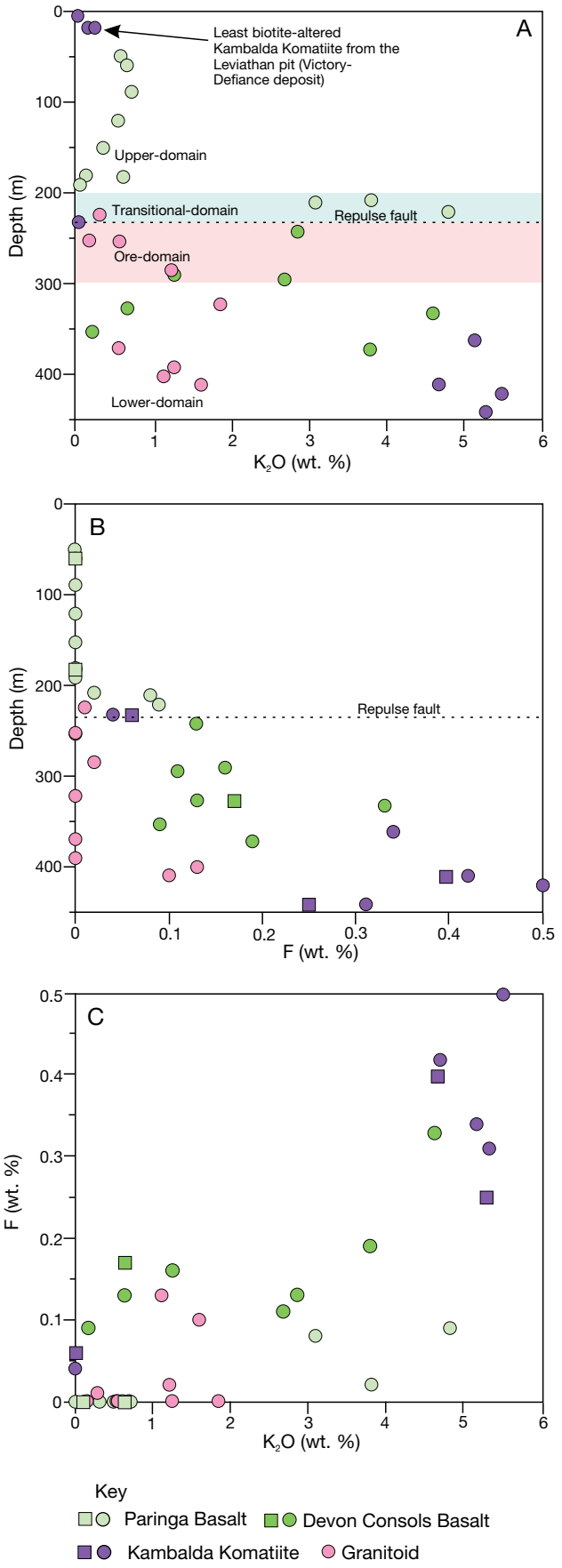

Paringa Basalt from the transitional domain contains lower F/K ratios than ore and lower domain mafic and ultramafic rocks. This trend is consistent with decreases in the F content of biotite between the lower and/or ore domains and the transitional domain. Upper domain Paringa Basalts have the lowest F/K ratio of mafic and ultramafic rocks, which is consistent with F-poor biotite in these rocks. Granitoids show highly variable F/K ratios, which likely reflect the presence of variable amounts of K-feldspar and biotite between samples.

Discussion

Metasomatic fluorine

Fluorine and K have been added to biotite-altered metabasalts and komatiites during potassic metasomatism. According to Aoki et al. (1981), unaltered theoliites typically contain 0.01 to 0.03 wt % F and less than 1 wt % K_2O. Least altered Paringa Basalts in the upper domain of the East Repulse have less than 0.7 wt % K_2O (Fig. 14A) and are within the range of regional least altered Paringa Basalts (e.g., 0.1–1 wt % K_2O; Said and Kerrich, 2009). Fluorine values in upper domain Paringa Basalt are below detection limit of 0.01 wt % and have low values when compared to typical theoliites. Transitional domain Paringa Basalts contain between 3 to 5 wt % K_2O, reflecting pervasive K metasomatism and the addition of significant amounts of potassium in parts of the hanging wall. Transitional domain rocks are also relatively enriched in F (0.02–0.09 wt % F). Given the relatively high amounts of F in biotite (>0.25 wt %), it is also likely that these rocks have gained some F during K metasomatism.

Biotite-amphibole–altered Kambalda Komatiite in the lower domain contains between 4.5 and 5.5 wt % K_2O (Fig. 14A). These values are significantly higher than regional Kambalda Komatiites, which generally have less than 0.1 wt % K_2O (Arndt and Lesher, 1992). Potassic metasomatism of Kambalda Komatiites in the lower domain resulted in the addition of F; with one sample containing 0.5 wt % F. Based on the available evidence it appears that lithologic controls on the amount of K and F for strongly biotite altered metabasalts

FIG. 14. A. Depth vs. the abundance of K_2O in various rock types from the East Repulse deposit and adjacent Leviathan pit. Transitional domain Paringa Basalts are significantly more enriched in K compared to least altered Paringa Basalts from the upper domain. Lower domain Kambalda Komatiites are significantly more enriched in K compared to least altered Kambalda Komatiite from the Leviathan pit and talc-chlorite-carbonate–altered Kambalda Komatiite from the transitional domain. B. Depth vs. F abundance for selected samples from the upper, transitional, granitoid, and lower domains. Lower domain basalts and ultramafics are enriched in F compare to their counterpart in the upper and transitional domains, respectively. C. F vs. K_2O showing lower domain Kambalda Komatiites have higher F:K ratios compared to rocks from the upper and transitional domains. This pattern is consistent with increasing fluorine in biotite with increasing depth (see Fig. 11C). Devon Consols Basalts have variable F/K ratios, which also likely reflects increasing fluorine in biotite with depth; however, some samples have more fluorine than can be account for by K (biotite) content, which indicates that phases (e.g., amphibole, epidote, and apatite) may contain much of the F in these samples. Granitoids contain very low amounts of F and there is no correlation between F and K, which is explained by the occurrence of K-feldspar phenocrysts in samples. Note that for plots involving fluorine, squares signify that the fluorine analysis was carried out by XRF, whereas circles signify that the F analysis was done by the ISE.

and komatiites were negligible. Our data shows that these elements are well above expected background values for theoliites and komatiites, and hence these elements were likely added to these rocks at the time of biotite alteration.

Temperature controls on fluorine variations in biotite

Whole-rock and biotite data support the contention that the most F rich fluids occurred in the lower domain and relatively F poor fluids occurred in the upper domain. However in theory, variations in the F composition of biotite could also be explained by temperature variations across the East Repulse deposits. A steep inverse temperature gradient of approximately 200°C over 200 m would be required to form F-poor biotite in the transitional and upper domains and F-rich biotites in the lower and granitoid domains at a constant fluid composition. Temperature constraints provided by biotite-apatite geothermometry yielded lower average temperatures between depths of 230 (~550°C) to 285 m (~450°C) consistent with an inverse temperature gradient. However as mentioned earlier these temperature estimates are all within error of each other.

We examined use of the Ti-in-biotite geothermometer, developed by Henry et al. (2005), to help identify possible thermal gradients across the East Repulse deposit. This geothermometer was developed for biotite in peraluminous metapelites with coexisting rutile, ilmenite, and graphite at 4 to 6 kbars pressure. The presence of graphite in the assemblage constrains low f_{O_2} and consequently Fe^{3+} in biotite to low and approximately constant amounts of ~12% Fe_{total} (Guidotti and Dyar 1991). Biotite from the ore and granitoid domains of the East Repulse deposit occurs with rutile and ilmenite (Fig. 8F), satisfying the requirement of Ti saturation, but as noted above the Fe^{3+}in biotite is likely to be relatively high and variable. Biotite in the upper and transition domains is associated with titanite, rather than ilmenite and rutile. No accessory Ti phases occur with biotite in the Kambalda Komatiite and their absence is consistent with low Ti contents of biotite from these rocks (Fig. 11B). The Ti-in-biotite geothermometer was applied to biotite of the ore and granitoid domain. Results yield an average temperature of 610° ± 60°C (1σ error) that is significantly higher than estimated using the biotite-apatite thermometer. The differences in absolute temperature estimates may reflect the oxidized conditions in the East Repulse deposit and uncertainties associated with the higher inferred Fe^{3+}in biotite compared with the system modeled by Henry et al. (2005). The Ti-in-biotite geothermometer provided no qualitative evidence for a thermal gradient between granitoids in the lower and ore domains at the time of main-stage biotite alteration. We conclude that variations in the abundance of F in biotite across the East Repulse deposit most likely reflect changes in the log $(f_{H_2O}/f_{HF})_{fluid}$ of metasomatic fluids as opposed to a temperature gradient.

Oxidized fluorine- and potassic-bearing fluids

The occurrence of F-rich biotite and anhydrite in the lower and granitoid domains of the East Repulse deposit link F and K metasomatism to an oxidized, sulfate-rich, fluid regime in the lower domain. This association persists into the ore domain, where traces of sulfate minerals (barite and celestine) occur as inclusions in pyrite associated with F-rich biotite (Fig. 5A, B), indicating that sulfate-bearing fluids were present in the core of the deposit. In the hanging wall of the deposit, sulfate minerals are rare. Minor pentlandite, millerite, siegenite, cobaltite, sphalerite, and trace galena occur with an assemblage of clinozoisite, pyrite, and pyrrhotite, indicating reduced rather than oxidized conditions in the transition and upper domains. Systematic changes in $\delta^{34}S$ values of sulfides between the footwall of the Repulse fault (–10–0‰ VCDT) and the hanging wall (0–5‰ VCDT), associated with the change from epidote to clinozoisite (Roache et al, 2011), are indicative of a switch from oxidized conditions in the footwall to reduced conditions in the hanging wall.

Some authors argue that redox gradients in major deposits such as the Golden Mile and the St. Ives camp arise from progressive oxidation of reduced fluids through fluid rock reactions. One suggested mechanism utilizes magnetite in wall rocks to trigger the oxidation (Lambert et al., 1984; Evans et al., 2006; Evans, 2010). Quartz-magnetite–rich rocks occur in the ore domain of the East Repulse deposit (Fig. 5B) and could provide the source of ferric iron needed to drive oxidation of reduced fluids. However, our data show that the most oxidized assemblages are not centered on the quartz-magnetite–rich rocks but occur lower in the section within the granitoids and the Kambalda Komatiite of the lower domain. The quartz-magnetite–rich rocks mark a transition from sulfate-rich assemblages of the lower domain to sulfide-rich rocks of the ore domain.

Alteration zonation, pathways, and sources of fluids

As noted by a number of authors (Gunow et al., 1980; Markl and Piazolo, 1998; Aksyuk, 2002; Boomeri et al., 2009, 2010), F, unlike Cl, preferentially partitions into mineral phases during fluid-rock interaction and may be depleted in the fluid over relatively short transport distances. Domains of high f_{HF} relative to f_{H_2O} should represent domains of least evolved fluid that have retained most source characteristics, including their redox properties that are also likely to be readily degraded through fluid-rock reaction and fluid-mixing. Systematic changes in F concentrations in biotite and other phases may provide a tool to track pathways of highly oxidized fluids. Sharp gradients in the fugacity of HF in fluids could be used to define the boundaries of pathways of oxidized, F-bearing fluids. In the East Repulse deposit example, the focus of oxidized fluid appears to have been the granitoid domain below the deposit with the fugacity of HF decreasing through fluid-rock reaction, fluid-mixing, or possibly degassing as fluids migrated upward.

The pathways may have been internal to the granitoids. Albite-altered granitoids contain abundant micropores (<20 μm), which in places are partly filled with barite, pyrite (with electrum inclusions), carbonate, and biotite (Fig. 7D, F). The micropores appear in zones of albitization of relatively Ca rich feldspar and appear similar to those described by other authors (e.g., Engvik et al., 2008; Putnis, 2009; Hovelmann et al., 2010). Micropores were generated in albite-altered granitoids during early-stage albite alteration that commonly overprints a deformation fabric. Increased permeability of steeply dipping dikes may have provided pathways for oxidized fluids to migrate upward during main-stage biotite alteration. Fluids could have also migrated along the contact between the granitoid dikes and mafic or ultramafic wall rocks, as some mineralized zones have elevated gold along the contact of the granitoids.

Detailed work using the scanning electron microscope revealed that many granitoids beneath the ore domain have assemblages of celestine, Ce monazite, barite, galena, bismuthinite, molybdenite, and scheelite, whereas adjacent Kambalda Komatiite and Devon Consols Basalt only in part contain these phases in the lower domain. Elsewhere, these minerals are only common in the ore domain where they occur in a wide variety of different rock types. This commonality of mineral assemblages, together with gold occurrences in the altered granitoids that have intruded lower domain rocks, provides an additional connective link with the ore domain.

The source of oxidized fluids is impossible to identify based on the current dataset. However the sharp increase in $\log(f_{H_2O}/f_{HF})$ of fluids in equilibrium with biotite over short vertical distances appears inconsistent with processes involving fluid-rock equilibration over large transport distances. Oxidized, F-rich, low-salinity potassic fluids and/or volatiles may have been derived from proximal magmatic sources beneath the East Repulse at the time of gold mineralization.

Conclusions

The F content of biotite has been used to identify the pathway and flow direction of sulfate-rich potassic fluids in the footwall of the East Repulse deposit. A systematic decrease in F abundance and increase in the $\log (f_{H_2O}/f_{HF})_{fluids}$ is consistent with oxidized fluids migrating upward along contacts between steeply dipping granitoid dikes and mafic and/or ultramafic wall rocks which show pervasive biotite-amphibole-sulfate alteration. Oxidized-potassic fluids may have also migrated through steeply dipping granitoid dikes, which exhibit porosity that was developed during an earlier albite-carbonate alteration event where andesine and/or oligoclase was replaced by albite. Sulfur in these fluids became progressively more reduced promoting the precipitation of sulfides over anhydrite, barite and/or celestine.

Evidence for fluids moving along granitoid dikes is supported by the occurrence of elevated gold in these intrusions beneath the ore domain and a correlation of minor mineral phases (e.g., scheelite, monazite, barite, and celestine) in the granitoids at depth with altered rocks in the ore domain. The addition of significant amounts of K and F to rocks in the lower domain is also evidence that K- and F-bearing fluids interacted with wall rocks in the lower domain.

Geothermometry of main-stage biotite-apatite alteration in the ore, transitional, and granitoid domains has yielded temperatures of 480° ± 60°C. Our data have demonstrated that F in biotite and apatite can be useful in determining pathways of oxidized fluids that are related to gold mineralization. This dataset along with the alteration zonation patterns recorded here could be used to vector toward structures that host mineralization and may be a particularly useful targeting tool in systems that have been rotated.

Acknowledgments

We wish to thank St. Ives Gold Mining Company, Gold Fields Limited, Minerals and Energy Research Institute of Western Australia, M410 project sponsors and the CSIRO Minerals Down Under National Research Flagship for financial and logistical support. A special thanks also goes to all the staff from St. Ives Gold Mining Company who provided logistical and intellectual support toward this project, particularly John Donaldson, Julian Woodcock, Christopher Lusty, Colby Simonis, Ayesha Ahmed, and Paps. We are grateful for the feedback provided by Chris Yeats, Camilla Myers, and Iris Sonntage (all CSIRO) on earlier versions of the manuscript. Reviews from Jeremy Richards and an anonymous reviewer, as well as comments by John Dilles helped to improve the content of the manuscript significantly.

REFERENCES

Aksyuk, A.M., 2002, Experimentally established geofluorimeters and the fluorine regime in granite-related fluids: Petrology, v. 10, p. 557–569.

Andersen, T., and Austrheim, H., 1991, Temperature HF fugacity trends during crystallization of calcite carbonatite magma in the Fen complex, Norway: Mineralogical Magazine, v. 55, p. 81–94.

Anthony, E.Y., and Titley, S.R., 1988, Progressive mixing of isotopic reservoirs during magma genesis at the Sierrita porphyry copper-deposit, Arizona—inverse solutions: Geochimica et Cosmochimica Acta, v. 52, p. 2235–2249.

Aoki, K., Ishiwaka, K., and Kanisawa, S., 1981, Fluorine geochemistry of basaltic rocks from continental and oceanic regions and petrogenetic application: Contributions to Mineralogy and Petrology, v. 76, p. 53–59.

Arndt, N.T., and Lesher, C.M., 1992, Fractionation of REEs by olivine and the origin of Kambalda Komatiites, Western Australia: Geochimica et Cosmochimica Acta, v. 56, p. 4191–4204.

Bateman, R., and Hagemann, S., 2004, Gold mineralisation throughout about 45 Ma of Archaean orogenesis: Protracted flux of gold in the Golden Mile, Yilgarn craton, Western Australia: Mineralium Deposita, v. 39, p. 536–559.

Beane, R.E., 1974, Biotite stability in porphyry copper environment: Economic Geology, v. 69, p. 241–256.

Binder, G., and Troll, G., 1989, Coupled anion substitution in natural carbon-bearing apatites: Contributions to Mineralogy and Petrology, v. 101, p. 394–401.

Bird, D.K., and Helgeson, H.C., 1980, Chemical interaction of aqueous solutions with epidote-feldspar mineral assemblages in geologic systems. 1 Thermodynamic analysis of phase relations in the system CaO-FeO-Fe_2O_3-Al_2O_3-SiO_2-H_2O-CO_2: American Journal of Science, v. 280, p. 907–941.

——1981, Chemical interaction of aqueous solutions with epidote-feldspar mineral assemblages in geologic systems. II. Equilibrium constraints in metamorphic/geothermal processes: American Journal of Science, v. 281, p. 576–614.

Blewett, R.S., Squire, R., Miller, J.M., Henson, P.A., and Champion, D.C., 2010, Architecture and geodynamic evolution of the St. Ives goldfield, eastern Yilgarn craton, Western Australia: Precambrian Research, v. 183, p. 275–291.

Boomeri, M., Nakashima, K., and Lentz, D.R., 2009, The Miduk porphyry Cu deposit, Kerman, Iran: A geochemical analysis of the potassic zone including halogen element systematics related to Cu mineralization processes: Journal of Geochemical Exploration, v. 103, p. 17–29.

Boomeri, M., Nakashima, K., and Lentz, D.R., 2010, The Sarcheshmeh porphyry copper deposit, Kerman, Iran: A mineralogical analysis of the igneous rocks and alteration zones including halogen element systematics related to Cu mineralization processes: Ore Geology Reviews, v. 38, p. 367–381.

Camp, J.K., 2011, Late Archean felsic intrusions and their link to mineralization at St. Ives gold camp, Western Australia: Unpublished Honours thesis, Monash University, 40 p.

Clark, M.E., Carmicheal, D.M., Hodgson, C.J., and Fu, M., 1989, Wall-rock alteration, Victory gold mine, Kambalda, Western Australia: Processes and P-T-$X_{(CO_2)}$ conditions of metasomatism: Economic Geology Monograph 6, p. 445–456.

Cleverley, J. S., 2006, Using the chemistry of apatite to track fluids in Fe-oxide Cu-Au systems [abs.]: Annual V.M. Goldschmidt Conference, 16th, Melbourne, 2006, Abstracts, p. A105.

Cox, S.F., and Ruming, K., 2004, The St. Ives mesothermal gold system, Western Australia—a case of golden aftershocks?: Journal of Structural Geology, v. 26, p. 1109–1125.

Czarnota, K., Champion, D.C., Goscombe, B., Blewett, R.S., Cassidy, K.F., Henson, P.A., and Groenewald, P.B., 2010, Geodynamics of the eastern Yilgarn craton: Precambrian Research, v. 183, p. 175–202.

Dilles, J.H., and Einaudi, M.T., 1992, Wall-rock alteration and hydrothermal flow paths about the Ann-Mason porphyry copper deposit, Nevada—a 6-km vertical reconstruction: Economic Geology, v. 87, p. 1963–2001.

Engvik, A.K., Putnis, A., Gerald, J.D.F., and Austrheim, H., 2008, Albitization of granitic rocks: the mechanism of replacement of oligoclase by albite: Canadian Mineralogist, v. 46, p. 1401–1415.

Evans, K.A., 2010, A test of the viability of fluid-wall rock interaction mechanisms for changes in opaque phase assemblage in metasedimentary rocks in the Kambalda-St. Ives goldfield, Western Australia: Mineralium Deposita, v. 45, p. 207–213.

Evans, K.A., Phillips, G.N., and Powell, R., 2006, Rock-buffering of auriferous fluids in altered rocks associated with the Golden Mile-style mineralization, Kalgoorlie gold field, Western Australia: Economic Geology, v. 101, p. 805–817.

Feldstein, S.N., Lange, R.A., Vennemann, T., and ONeil, J.R., 1996, Ferric-ferrous ratios, H_2O contents and D/H ratios of phlogopite and biotite from lavas of different tectonic regimes: Contributions to Mineralogy and Petrology, v. 126, p. 51–66.

Groves, D.I., Goldfarb, R.J., Gebre-Mariam, M., Hagemann, S.G., and Robert, F., 1998, Orogenic gold deposits: A proposed classification in the context of their crustal distribution and relationship to other gold deposit types: Ore Geology Reviews, v. 13, p. 7–27.

Groves, D.I., Goldfarb, R.J., Robert, F., and Hart, C.J.R., 2003, Gold deposits in metamorphic belts: Overview of current understanding, outstanding problems, future research, and exploration significance: Economic Geology, v. 98, p. 1–29.

Groves, D.I., Condie, K.C., Goldfarb, R.J., Hronsky, J.M.A., and Vielreicher, R.M., 2005, Secular changes in global tectonic processes and their influence on the temporal distribution of gold-bearing mineral deposits: Economic Geology, v. 100, p. 203–224.

Gunow, A.J., Ludington, S., and Munoz, J.L., 1980, Fluorine in micas from the Henderson molybdenite deposit, Colorado: Economic Geology, v. 75, p. 1127–1137.

Guidotti, C.V., and Dyar, M.D., 1991, Ferric iron in metamorphic biotite and its petrologic and crystallochemical implications: American Mineralogist, v. 76, p. 161–175.

Henry, D.J., Guidotti, C.V., and Thomson, J.A., 2005, The Ti-saturation surface for low-to-medium pressure metapelitic biotites: Implications for geothermometry and Ti-substitution mechanisms: American Mineralogist, v. 90, p. 316–328.

Hovelmann, J., Putnis, A., Geisler, T., Schmidt, B.C., and Golla-Schindler, U., 2010, The replacement of plagioclase feldspars by albite: Observations from hydrothermal experiments: Contributions to Mineralogy and Petrology, v. 159, p. 43–59.

Hutchison, R., 2011, Geology and definition of the Wattle Dam coarse gold deposit: The AusIMM Bulletin, no. 4, p. 49–55.

Kerrich, R., Goldfarb, R., Groves, D., Garwin, S., and Jia, Y., 2000, The characteristics, origins, and geodynamic settings of supergiant gold metallogenic provinces: Science in China Series D, Earth Sciences, v. 43, p. 1–68.

Kositcin, N., Brown, S.J.A., Barley, M.E., Krapez, B., Cassidy, K.F., and Champion, D.C., 2008, SHRIMP U-Pb zircon age constraints on the Late Archaean tectonostratigraphic architecture of the Eastern Goldfields superterrane, Yilgarn craton, Western Australia: Precambrian Research, v. 161, p. 5–33.

Lambert, I.B., Phillips, G.N., and Groves, D.I., 1984, Sulphur isotope compositions and genesis of Archaean gold mineralization, Australia and Zimbabwe, *in* Foster, R. P., ed., Gold '82: The geology, geochemistry and genesis of gold deposits: Rotterdam, A.A. Balkema, p. 373–387.

Markl, G., and Piazolo, S., 1998, Halogen-bearing minerals in syenites and high-grade marbles of Dronning Maud Land, Antarctica: Monitors of fluid compositional changes during late-magmatic fluid-rock interaction processes: Contributions to Mineralogy and Petrology, v. 132, p. 246–268.

Miller, J., Blewett, R., Tunjic, J., and Connors, K., 2010, The role of early formed structures on the development of the world class St. Ives goldfield, Yilgarn, WA: Precambrian Research, v. 183, p. 292–315.

Munoz, J.L., 1984, F-OH and Cl-OH exchange in micas with applications to hydrothermal ore-deposits: Reviews in Mineralogy, v. 13, p. 469–493.

——1992, F and Cl contents of hydrothermal biotites: A reevaluation [abs.]: Geological Society of America Abstract with Programs, v. 22, p. A135.

Munoz, J.L., and Ludington, S., 1977, Fluorine-hydroxyl exchange in synthetic muscovite and its application to muscovite-biotite assemblages: American Mineralogist, v. 62, p. 304–308.

Munoz, J.L., and Swenson, A., 1981, Chloride-hydroxyl exchange in biotite and estimation of relative HCl/HF activities in hydrothermal fluids: Economic Geology, v. 76, p. 2212–2221.

Nelson, D.R., 1997, Evolution of the Archaean granite-greenstone terranes of the eastern goldfields, Western Australia: SHRIMP U-Pb zircon constraints: Precambrian Research, v. 83, p. 57–81.

Neumayr, P., Walshe, J., Hagemann, S., Petersen, K., Roache, A., Frikken, P., Horn, L., and Halley, S., 2008, Oxidized and reduced mineral assemblages in greenstone belt rocks of the St. Ives gold camp, Western Australia: Vectors to high-grade ore bodies in Archaean gold deposits?: Mineralium Deposita, v. 43, p. 363–371.

Parry, W.T., and Jacobs, D.C., 1975, Fluorine and chlorine in biotite from Basin and Range plutons: Economic Geology, v. 70, p. 554–558.

Piccoli, P., and Candela, P., 1994, Apatite in felsic rocks—a model for the estimation of initial halogen concentrations in the Bishop Tuff (Long Valley) and Tuolumne Intrusive Suite (Sierra-Nevada batholith) magmas: American Journal of Science, v. 294, p. 92–135.

Prendergast, K., 2007, Application of lithogeochemistry to gold exploration in the St. Ives goldfield, Western Australia: Geochemistry-Exploration Environment Analysis, v. 7, p. 99–108.

Putnis, A., 2009, Mineral replacement reactions: Thermodynamics and Kinetics of Water-Rock Interaction, v. 70, p. 87–124.

Roache, T.J., Walshe, J.L., Huntington, J.F., Quigley, M.A., Yang, K., Bil, B.W., Blake, K.L., and Hyvarinen, T., 2011, Epidote-clinozoisite as a hyperspectral tool in exploration for Archean gold: Australian Journal of Earth Sciences, v. 58, p. 813–822.

Said, N., and Kerrich, R., 2009, Geochemistry of coexisting depleted and enriched Paringa Basalts, in the 2.7 Ga Kalgoorlie terrane, Yilgarn craton, Western Australia: Evidence for a heterogeneous mantle plume event: Precambrian Research, v. 174, p. 287–309.

Samson, I.M., Blackburn, W.H., and Gagnon, J.E., 1999, Paragenesis and composition of amphibole and biotite in the MacLellan gold deposit, Lynn Lake greenstone belt, Manitoba, Canada: Canadian Mineralogist, v. 37, p. 1405–1421.

Squire, R.J., Allen, C.M., Cas, R.A.F., Campbell, I.H., Blewett, R.S., and Nemchin, A.A., 2010, Two cycles of voluminous pyroclastic volcanism and sedimentation related to episodic granite emplacement during the Late Archean: Eastern Yilgarn craton, Western Australia: Precambrian Research, v. 183, p. 251–274.

Swager, C.P., 1997, Tectono-stratigraphy of late archaean greenstone terranes in the southern Eastern goldfields, Western Australia: Precambrian Research, v. 83, p. 11–42.

Tacker, R.C., and Stormer, J.C., 1989, A thermodynamic model for apatite solid-solutions, applicable to high-temperature geologic problems: American Mineralogist, v. 74, p. 877–888.

Watchorn, R.B., 1998, Kambalda-St. Ives gold deposits, *in* Berkman, D. A., and Mackenzi, D. H., eds., Geology of Australia and Papua New Guinean mineral deposits: Melbourne, Australasian Institute of Mining and Metallurgy, p. 243–254.

Webster, J.D., 1997, Exsolution of magmatic volatile phases from Cl-enriched mineralizing granitic magmas and implications for ore metal transport: Geochimica et Cosmochimica Acta, v. 61, p. 1017–1029.

——2004, The exsolution of magmatic hydrosaline chloride liquids: Chemical Geology, v. 210, p. 33–48.

Webster, J.D., Tappen, C.M., and Mandeville, C.W., 2009, Partitioning behavior of chlorine and fluorine in the system apatite-melt-fluid. II: Felsic silicate systems at 200 MPa: Geochimica et Cosmochimica Acta, v. 73, p. 559–581.

Weinberg, R.F., and van der Borgh, P., 2008, Extension and gold mineralization in the Archean Kalgoorlie terrane, Yilgarn craton: Precambrian Research, v. 161, p. 77–88.

Weinberg, R.F., Hodkiewicz, P.F., and Groves, D.I., 2004, What controls gold distribution in Archean terranes?: Geology, v. 32, p. 545–548.

Weinberg, R.F., Van der Borgh, P., Bateman, R.J., and Groves, D.I., 2005, Kinematic history of the Boulder-Lefroy shear zone system and controls on associated gold mineralization, Yilgarn craton, Western Australia: Economic Geology, v. 100, p. 1407–1426.

Yeats, C.J., McNaughton, N.J., Ruettger, D., Bateman, R., Groves, D.I., Harris, J.L., and Kohler, E., 1999, Evidence for diachronous Archean lode gold mineralization in the Yilgarn craton, Western Australia: A SHRIMP U-Pb study of intrusive rocks: Economic Geology, v. 94, p. 1259–1276.

Zhu, C., and Sverjensky, D.A., 1991, Partitioning of F-Cl-OH between minerals and hydrothermal fluids: Geochimica et Cosmochimica Acta, v. 55, p. 1837–1858.

——1992, F-Cl-OH partitioning between biotite and apatite: Geochimica et Cosmochimica Acta, v. 56, p. 3435–3467.